Progress in Oceanography 193 (2021) 102548

Contents lists available at ScienceDirect

Progress in Oceanography

journal homepage: www.elsevier.com/locate/pocean

A local eddy viscosity parameterization for wind-driven estuarine exchange flow. Part I: Stratification dependence

N. Berkay Basdurak [a,b,*], Hans Burchard [a], Henk M. Schuttelaars [c]

[a] Leibniz Institute for Baltic Sea Research Warnemünde, Seestr. 15, D-18119, Rostock, Germany
[b] Institute of Marine Sciences, Middle East Technical University, Erdemli, Turkey
[c] Delft Institute of Applied Mathematics, Delft University of Technology, Delft, Netherlands

ARTICLE INFO

Keywords:
Wind driven exchange flow
Eddy viscosity coefficient
Estuarine dynamics
Analytical techniques
Density stratification
Parameterization properties

ABSTRACT

A new parameterization for the estuarine turbulent eddy viscosity coefficient is developed considering the influence of wind forcing and feedback between stratification and shear. The emerging tidally averaged eddy viscosity profile A_v^T is parameterized as parabolic under well-mixed conditions, and is composed of a skewed-Gaussian-like form for the upper layer, and a parabolic form for the bottom layer under stratified conditions. The precise shape of the profiles depends parametrically on the bottom boundary layer thickness, the bulk Richardson number, and the Wedderburn number. The parameterized A_v^T profiles show excellent agreement with profiles obtained from numerical models. To explore the importance of vertically varying A_v^T with regard to exchange processes, an analytical model is designed. This one-dimensional model is based on a balance between frictional forces and pressure gradient. The resulting exchange flow is analyzed over the relevant parameter space that is associated with horizontal and vertical stratification through the bulk Richardson number, and the bi-directional wind stress via the Wedderburn number. Down-estuary wind enhances the up-estuary flow near the bottom and down-estuary flow near the surface driving an exchange flow pattern typically associated with gravitational circulation. Up-estuary wind results in either a two-layer inverted circulation opposing the gravitational circulation, or a three-layer flow that is up-estuarine at the surface with classical two-layer circulation underneath. Three-layer flow emerges with a weak wind. With increasing runoff velocity, three-layer flow transitions to a single layer flow under weak stratification conditions.

1. Introduction

Estuarine circulation is defined as the subtidal longitudinal flow in an estuarine cross-section. Commonly a two-layered structure is observed, with a persistent inflow of water near the bottom and outflow above. This flow is potentially responsible for exchanging water between the estuary and the ocean (Geyer and MacCready, 2014); thus referred to as the exchange flow. The exchange flow is set by a balance between buoyancy forcing and turbulent mixing of momentum associated with barotropic tides, river run-off, advection, and wind forcing. In tidally energetic systems, significant contributions to the estuarine circulation can be generated by tidal covariance of eddy viscosity and velocity shear (i.e., eddy viscosity shear covariance ESCO, Dijkstra et al. (2017)) due to tidal asymmetry in both magnitude and shape of eddy viscosity. Strain-induced periodic stratification (Simpson et al., 1990), is one of the physical mechanisms that generates ESCO, and it contributes significantly to the circulation in tidally energetic systems (Burchard et al., 2011; Cheng et al., 2011; Geyer and MacCready, 2014).

Estuarine stratification is sensitive to directional wind stress as it modifies turbulent mixing within the water column via direct mixing or straining (the former effect scales with the local Wedderburn number W, the ratio of wind stress and local stratifying forces, and the latter scales with the Simpson number S_i representing the dimensionless estuarine buoyancy gradient (Stacey et al., 2010; Dijkstra et al., 2017; Lange and Burchard, 2019)). Down-estuary winds can enhance the exchange flow (Ralston et al., 2008; Chen and Sanford, 2009; Burchard and Hetland, 2010; Purkiani et al., 2016), whereas up-estuary winds suppress and even invert (Lange and Burchard, 2019) it.

To accurately model the strength and structure of the exchange flow, a spatially and temporally varying description of the eddy viscosity profile is essential. Numerical (Geyer et al., 2000; Cheng et al., 2013) and observational studies (Chant et al., 2007; Basdurak et al., 2017) point to intricate eddy viscosity profiles showing enhanced vertical and temporal variability with stratification. They reveal that with enhanced stratification, the eddy viscosity not only gets weaker in

* Corresponding author at: Institute of Marine Sciences, Middle East Technical University, Erdemli, Turkey.
E-mail address: berkay.basdurak@io-warnemuende.de (N.B. Basdurak).

https://doi.org/10.1016/j.pocean.2021.102548
Received 6 November 2020; Received in revised form 7 February 2021; Accepted 1 March 2021
Available online 5 March 2021

magnitude, the maximum eddy viscosity is found at greater depths as well. The shift to greater depths is related to a change in boundary layer thickness.

The sensitivity of the exchange flow to stratification is systematically investigated using idealized description of the water motion. Over the last decades, the exchange flow has been studied using eddy viscosity profiles with increasing complexity. Classical solutions for the exchange flow by Hansen and Rattray (1965) are based on a vertical eddy viscosity that is constant in time and space. Later, these solutions have been extended to include parabolic eddy viscosity profiles (McGregor, 1972; Ianniello, 1977; Burchard and Hetland, 2010; Zitman and Schuttelaars, 2012; Lange and Burchard, 2019). Chen and De Swart (2016) have extended the eddy viscosity parameterization to depend on boundary layer thickness. However, the existing solutions for stratified exchange flow with eddy viscosity profiles that are more complex than parabolic and temporal, rely on numerical models.

In stratified systems, a parameterization for eddy viscosity with flexible spatial and temporal variability that accounts for the feedback from stratification, yet simple enough to implement into analytical models allows for extensive sensitivity studies. Moreover, in the context of wind driven circulation, a relatively small portion of W - S_i parameter space has been explored by numerical models due to runaway stratification, and by analytical models due to the lack of vertical–horizontal stratification interaction in formulating eddy viscosity.

In view of this, the aims of this article are twofold: (I) to develop a physically driven subtidal eddy viscosity parameterization that considers the influence of vertical stratification interacting with the along-estuary buoyancy gradient; (II) to gain insight in estuarine exchange flow structure and its dependence on the eddy viscosity parameterization by using a novel analytical method. In this newly developed eddy viscosity parameterization, a parabolic profile close to the bed represents the well-mixed logarithmic part of the bottom boundary layer, whereas the degree of stratification determines the shape of the upper part and the bottom boundary layer thickness. Using these parameters of the eddy viscosity profiles, neglecting Coriolis and non-linear advection, analytical solutions are derived for gravitational and wind-driven exchange flow, and the W - S_i parameter space is explored using the analytical model results with a specific focus on the exchange flow.

The paper is organized as follows. In Section 2, the dynamical equation and the new model for the eddy viscosity will be presented. In Section 3, the eddy viscosity parameterization is validated using numerical model results. Using the new parameterization, the analytical solution for the exchange flow will be derived in Section 4. In Section 5, solutions for the exchange flow under varying axial and bi-directional wind forcing, and stratification will be investigated and mapped in the W - S_i parameter space. Finally, the results will be discussed in Section 6.

2. Model description

2.1. Dynamical equation

The one-dimensional tidally-averaged dynamic equation in along-channel direction consists of a balance between pressure gradient and friction. Assuming that the longitudinal buoyancy gradient is constant in time and space, and ignoring earth's rotation and nonlinear advection, the resulting tidally-averaged equation reads

$$\partial_z \left(A_v^T \partial_z u\right) = z\partial_x B + P_x/\rho_0, \tag{1}$$

where x and z denote longitudinal and downward Cartesian coordinates; A_v^T is the tidally averaged eddy viscosity, $\partial_x B$ is the prescribed buoyancy gradient with buoyancy $B = -g\left(\rho - \rho_0\right)/\rho_0$ and the reference density $\rho_0 = 1000$ kg m^{-3}; P_x is the tidally-averaged external pressure gradient induced by the surface slope. Given the residual depth-mean runoff velocity u_r, P_x is obtained through the constraint $\int_{-H}^{0} u(z)\,dz = Hu_r$ with water depth H (Burchard and Hetland, 2010). Boundary conditions are a no-slip condition at the bottom, and a rigid-lid at the surface with a prescribed momentum flux based on the wind stress τ_s and its direction:

$$u(z=-H) = 0, \quad \text{and} \quad \partial_z u(z=0) = \frac{\tau_s}{\rho_0 A_v^T} = \frac{u_*^s\left|u_*^s\right|}{A_v^T}. \tag{2}$$

In (2), u_*^s is the directional surface friction velocity. As motivated in the Introduction, an improved parameterization has to be developed to capture the complex depth dependent structure of A_v^T. For that, two layers, the top and bottom layer, will be parameterized independently. By requiring that their values and their first derivative are identical at the depth where the two layers merge, a continuous and differentiable eddy viscosity profile over depth is obtained. Below, the parameterization of the near-bed eddy viscosity is discussed, followed by the eddy viscosity parameterization of the top layer.

2.2. Eddy viscosity parameterization

Observational and numerical studies on the bottom boundary layer (BBL) characteristics suggest that the local maximum of eddy viscosity generally occurs near the middle of the BBL. To indicate these BBL characteristics, the parabolic eddy viscosity formulation by Burchard and Hetland (2010) is modified to include the BBL thickness h_b; the eddy viscosity for the bottom layer reads $A_v^{T_L}$

$$A_v^{T_L} = \kappa\left|u_*^b\right|\left(H + z + z_0^b\right)\left(1 - \frac{z+H}{h_b + z_0^b}\right) \qquad -H \le z \le z_m. \tag{3}$$

Here, $\kappa = 0.4$, u_*^b, and z_0^b are the van Kármán constant, the bottom friction velocity, and the bottom roughness length, respectively, with $z_m = h_b/2 - H$, the depth that corresponds to the local maximum i.e., $\partial_z A_v^{T_L}|_{z=z_m} = -2\kappa\left|u_*^b\right|\left(z - z_m\right)/\left(h_b + z_0\right)|_{z=z_m} = 0$. The log-law of the wall is preserved in this part of the BBL by keeping the profile parabolic regardless of stratification. Under the assumptions that the whole water column is well-mixed (i.e., $h_b = H$), and $z_0^b \ll h_b$, (1) reduces to the classical parabolic profile. The local maximum of $A_v^{T_L}$ scales with $\kappa u_*^b\left(h_b/2 + z_0^b\right)^2/\left(h_b + z_0^b\right) \approx \kappa u_*^b h_b/4$ for $z_0^b \ll h_b$; and is equal to $\kappa u_*^b H/4$ for the classical parabolic profile. Eq. (1) provides a simple, yet effective formulation in keeping the lower part of the bottom layer mixed so that the fully turbulent nature of the near-wall region is preserved. When z approaches $-H$, $A_v^{T_L} \to \kappa|u_*^b|z_0^b$, independent of h_b, to comply with the log-law of the wall.

Now we consider the upper layer; the formulation of the eddy viscosity in this layer reads

$$A_v^{T_U} = \left[\kappa\left|u_*^b\right|\frac{\left(h_b/2 + z_0^b\right)^2}{\left(h_b + z_0^b\right)} - \kappa\left|u_*^s\right|z_0^s\right]\xi(z,\alpha,\beta) + \kappa\left|u_*^s\right|z_0^s \qquad z_m \le z \le 0. \tag{4}$$

Here, z_0^s is the surface roughness length and $\xi(z,\alpha,\beta)$ is a shape function. The superscript T_U denotes the top layer where stratified conditions are allowed. To capture a wide range of A_v profiles ranging from parabolic to Gaussian above the fully turbulent part of the BBL ($z_m \le z \le 0$), the shape function ξ is chosen as a special form of the beta distribution:

$$\xi(z,\alpha,\beta) = \left(\frac{z}{z_m}\right)^{\alpha-1}\left(\frac{H+z}{H+z_m}\right)^{\beta-1}. \tag{5}$$

By varying the parameters α and β, the observed shapes of eddy viscosity can be well represented; the beta distribution is symmetric around its maximum for $\alpha = \beta$, positively skewed and negatively skewed for $\alpha < \beta$ and $\alpha > \beta$ (Fig. 1). At $z = 0$ and at $z = -H$, ξ is equal to 0. The shape parameter β is related to z_m and α as

$$\beta = (\alpha - 1)H/\left|z_m\right| - \alpha + 2, \tag{6}$$

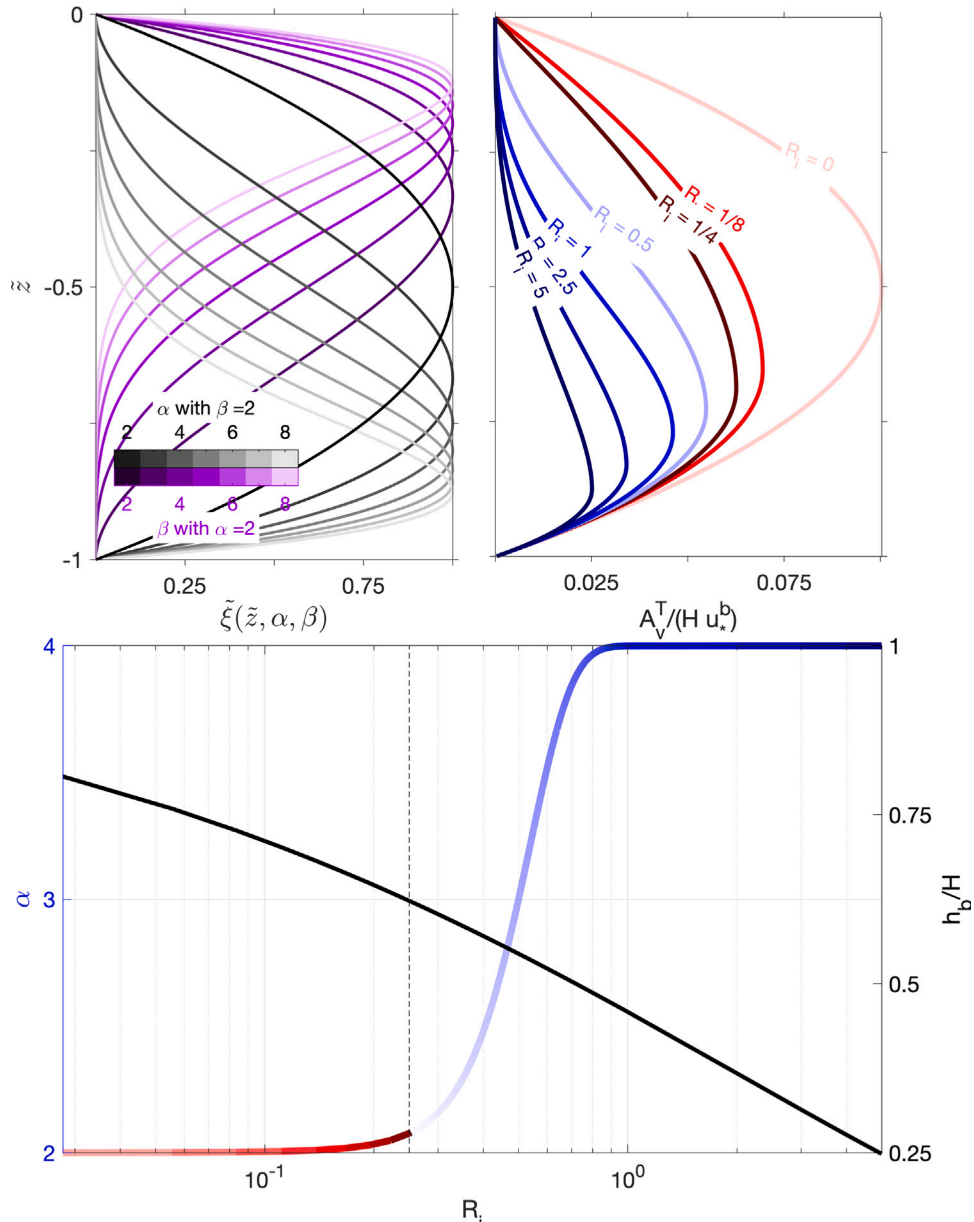

Fig. 1. Shape function ξ (Eq. (5)) with varying shape parameters α and β (top left panel). Non-dimensional eddy viscosity profiles under varying R_i (top right panel). Boundary layer thickness h_b (black line) and shape parameter α (Eq. (12); bottom panel); color denotes change in R_i with regards to critical $R_i = 0.25$ (marked as a dashed line), red for $R_i \leq 0.25$ and blue for $R_i > 0.25$. (For interpretation of the references to color in this figure legend, the reader is referred to the web version of this article.)

ensuring $\xi(z_m, \alpha, \beta) = 1$, and the vertical derivative of the shape function at $z = z_m$, $\partial_z \xi|_{z=z_m}$ is zero. Furthermore, the A_v profile is continuous at $z = z_m$, i.e., $A_v^{T_U}(z_m) = A_v^{T_L}(z_m)$.

By combining (3) and (4), the final form of the vertical eddy viscosity is found:

$$A_v^T = \begin{cases} A_v^{T_L} & -H \leq z \leq z_m \quad , \\ A_v^{T_U} & z_m < z \leq 0 \quad , \end{cases} \tag{7}$$

with A_v^T and its first derivative continuous over the depth; the maximum eddy viscosity is attained at $z = z_m$ where $\partial_z A_v^T|_{z=z_m} = 0$. At the surface and bottom, (7) results in $A_v^T(z=0) = \kappa \left|u_*^s\right| z_0^s$ and $A_v^T(z=-H) = \kappa \left|u_*^b\right| z_0^b$, respectively. In (7) wind entrainment is ignored. In other words, changes in surface boundary layer thickness with wind stress, and its effect on A_v^T, are not taken into account in the present study.

2.2.1. *Eddy viscosity coefficient A_v^T and stratification*

The sensitivity of A_v^T to stratification plays a key role in quantifying the estuarine exchange, and reduces its value from $\sim 500 \times 10^{-4}$ m^2 s^{-1} in unstratified, maximum tidal flow conditions (Dyer and Soulsby, 1988) to less than 1×10^{-4} m^2 s^{-1} within the stratified pycnocline (Peters and Bokhorst, 2001) by limiting the vertical length scale of turbulent eddies (Geyer and MacCready, 2014). To effectively scale the magnitude of A_v^T, the local stratification and rectification of the tide-induced shear should be accounted for. This can be achieved by linking the shape of the A_v^T profile to vertical and longitudinal stratification through h_b and α.

Vertical stratification is quantified by the estuarine bulk Richardson number $R_i = (g\Delta\rho/\rho_0)/(U_T^2/H)$ with the density difference between bottom and surface $\Delta\rho \geq 0$; the gravitational acceleration $g = 9.81$ m s^{-2}, and the velocity scale U_T (tidal current amplitude). Longitudinal stratification is quantified by the longitudinal Richardson number i.e., the Simpson number $S_i = H^2 \partial_x B / \left(u_*^b\right)^2$ (Simpson et al., 1990;

Monismith et al., 1996; Stacey et al., 2010; Burchard et al., 2011). These parameters describe the ratio of potential energy change due to straining to the rate of production of turbulent kinetic energy in vertical and longitudinal directions. The longitudinal density gradient $\partial_x B$ plays a key role in the coupled salt and momentum equations increasing with river flow and modifying the vertical shear. Here, R_i is chosen as the independent variable; it will be interlinked to S_i.

For smaller values of S_i and R_i, boundary layer mixing can extend through the water column. With increasing stratification i.e., higher values of S_i and R_i, the turbulent length scale decreases resulting in a decrease of the boundary layer thickness and the magnitude of the A_v^T, changing the shape of the A_v^T profile. Therefore both the curvature parameter α and h_b depend on stratification. In the following sections, explicit expressions for these parameters will be given in terms of stratification i.e., $\alpha(R_i)$ and $h_b(S_i, R_i)$.

2.2.2. Dependence of h_b on stratification

To relate h_b to the estuarine bulk Richardson number, R_i, we use the expression introduced by Chen and De Swart (2016). This relationship is based on observations from different estuaries, and reads

$$h_b = H \exp\left[-0.78 R_i^{0.36}\right] \tag{8}$$

When the water column is well mixed, h_b equals the water depth H. The upper limit for R_i is set to 5, and it corresponds to a minimum boundary layer thickness $h_b = H/4$ via (8).

2.2.3. Dependence of α on stratification

The curvature parameter α is related to the bulk Richardson number through the change in the turbulent length scale with stratification. Using bulk properties and assuming a constant buoyancy frequency N_∞ throughout the water column, the typical turbulent length scale l given in Taylor and Sarkar (2008) is approximated as a function of R_i

$$l = \left[\frac{1}{\kappa H} + \frac{N_\infty}{c_b\,|u_*^b|}\right]^{-1} \simeq \left\{ \left[\frac{1}{\kappa H} + \frac{\sqrt{R_i}}{H c_b}\right]^{-1}, \quad l_{lim} \right\}_{max}, \tag{9a}$$

$$l_{lim} = 5.87 \frac{\kappa z^r l_0}{\kappa z^r + l_0}, \quad \text{with} \quad l_0 = 0.17 h_b. \tag{9b}$$

When the water column is not stratified ($N_\infty = 0$ and $H = h_b$), the turbulent length scale reduces to κH. In (9a) the reduction in l with increasing stratification is defined in terms of R_i with a constant c_b. The constant c_b is obtained using a limiting condition for the turbulent length scale (9b) under maximum allowable stratification. To determine the maximum allowable length scale for stably stratified flows, numerical models apply a length scale clipping as an ad hoc remedy (Umlauf and Burchard, 2005). Following Canuto et al. (2001), l_{lim} is defined as a function of the reference depth z^r and h_b (valid for $l_{lim} \le q/2N_\infty$ with the turbulent kinetic energy q; Deardorff–Blackadar formula). Using the limits $R_i = 5$ and $h_b = H/4$ with $z^r = H$ results in $c_b = 1.15$.

Classical definitions of depth-independent eddy viscosity scale with the product of the friction velocity and the length scale. Because stratification modifies the boundary layer structure (i.e., well-mixed below the local maximum and stratified in the upper half of the BBL), (9) is used to show the change in bottom friction velocity. Using these definitions, the ratio of eddy viscosities under well mixed and stratified conditions can then be written as

$$\frac{\bar{A}_v}{\bar{A}_v^T} \propto \frac{u_*^b}{(u_*^b)_{\text{stratified}}}\frac{H}{h_b} = \frac{u_*^b \kappa H}{u_*^b l}\frac{1}{\tilde{h}_b} = \frac{C_0}{\tilde{h}_b}\left(1 + \frac{\kappa\sqrt{R_i}}{c_b}\right), \tag{10}$$

where $C_0 \sim 1$ is a constant, and $\tilde{h}_b = h_b/H$. With $\alpha = 2$ and $h_b = H$, $\bar{A}_v^T$ becomes identical to the parabolic eddy viscosity formulation A_v (Burchard and Hetland, 2010) for well mixed conditions. The overbar denotes depth-averaging so that $\bar{A}_v^T$ yields

$$\bar{A}_v^T = \frac{1}{H}\int_{h_b/2-H}^{0} A_v^{T_U}\,dz + \frac{1}{H}\int_{-H}^{h_b/2-H} A_v^{T_L}\,dz. \tag{11}$$

Using (8), (10) and (11) and assuming $z_0^b \ll h_b$ an implicit expression for α is found (see Appendix A). This h_b (thus R_i) dependent expression for α is then approximated as an error function by setting its lower (upper) limit as $\alpha = 2$ ($\alpha = 4$)

$$\alpha = erf\left(5R_i - 2.5\right) + 3. \tag{12}$$

Hereinafter, R_i will be used as the physical parameter with $\alpha = \alpha(R_i)$. For a fully mixed water column with $h_b = H$, corresponding to $R_i = 0$ ($\alpha = 2$), the A_v^T profile is parabolic. It is close to parabolic for $0 < R_i \le \frac{1}{4}$ ($\alpha \sim 2$) and skewed-Gaussian-like for $R_i > \frac{1}{4}$ ($2 < \alpha \le 4$), see Fig. 1b, c. The maximum change in shape occurs for $\frac{1}{4} < R_i < 1$. Only conditions with stable stratification are considered in this study ($R_i \ge 0$).

The R_i−dependent eddy viscosity parameterizations rely on constants that need to be adjusted to apply for estuarine settings; they yield underpredictions in mixing coefficient for small vertical velocity gradients. Models that use critical Richardson number (= 1/4) as a threshold for turbulence suppression often underpredict mixing and fail to predict the position of local eddy viscosity maxima in the water column. Therefore, incorporation of the bottom boundary layer length scale to the eddy viscosity parameterization provides a simple way to predict the position of near-bottom maximum; the depth associated with the change in its curvature. The R_i−dependence of the curvature accounts for how much the eddy viscosity profile gets deflected in the presence of stratification above the bottom boundary layer. Although classic stratified boundary layer theory, e.g., Monin–Obukhov, similarity scaling may account for the skewed mixing coefficient in the bottom boundary layer, it fails to describe the outer part; it performs better in a wall bounded flow regime.

3. Model validation

To test the validity of the A_v^T parameterization, the one dimensional water column model GOTM (General Ocean Turbulence Model, http://www.gotm.net) consisting of a $k - \epsilon$ model with algebraic second-moment closure (Umlauf and Burchard, 2005) is used. The resulting eddy viscosity profiles from GOTM and (7) are then compared to each other.

In GOTM, to simulate the estuarine circulation, a tidal current amplitude and a horizontal density gradient have to be prescribed. This entails introducing two new parameters for (7): the bulk drag coefficient $C_D = (u_*^b/U_T)^2$ which relates the tidal current amplitude U_T to u_*^b, and the Simpson number which has to be related to R_i.

First, the GOTM setup and the case studies are described. Second, C_D is parameterized in terms of R_i and compared to the GOTM runs. In addition to the GOTM simulations, data from recent DNS (Direct Numerical Simulation) studies and observational laboratory work are used to derive an empirical expression for h_b in terms of S_i. The upper and lower limits for h_b/H, R_i and S_i are discussed based on this dataset. Finally, the stratified eddy viscosity profiles resulting from (7) are compared to the model output.

3.1. GOTM setup

To explore the influence of the degree of stratification, an idealized scenario is set up with the tidal forcing (M_2 tide of period 12.42 h). The depth-averaged tidal current amplitude is prescribed as $U_T^0 = 0.39$ m s^{-1} (the superscript ^{0} is associated with prescribed parameters in the GOTM experiments). For GOTM input, the horizontal salinity gradient is calculated using the prescribed Simpson number S_i^0 and the U_T^0−dependent friction velocity $u_*^{b^0}$, with C_D (Burchard et al., 2011) related to a logarithmic velocity profile extending throughout the water column. The prescribed Si^0 is then rescaled by u_*^b (tidal-mean GOTM output) to find the actual $S_i = S_i^0(u_*^{b^0}/u_*^b)^2$ (Lange and Burchard, 2019).

Case studies include S_i varying between 0.12 – 0.23 with 0.05 increments, 0.3 – 1.5 with 0.15 increments, and 1.51 – 1.54 with 0.01

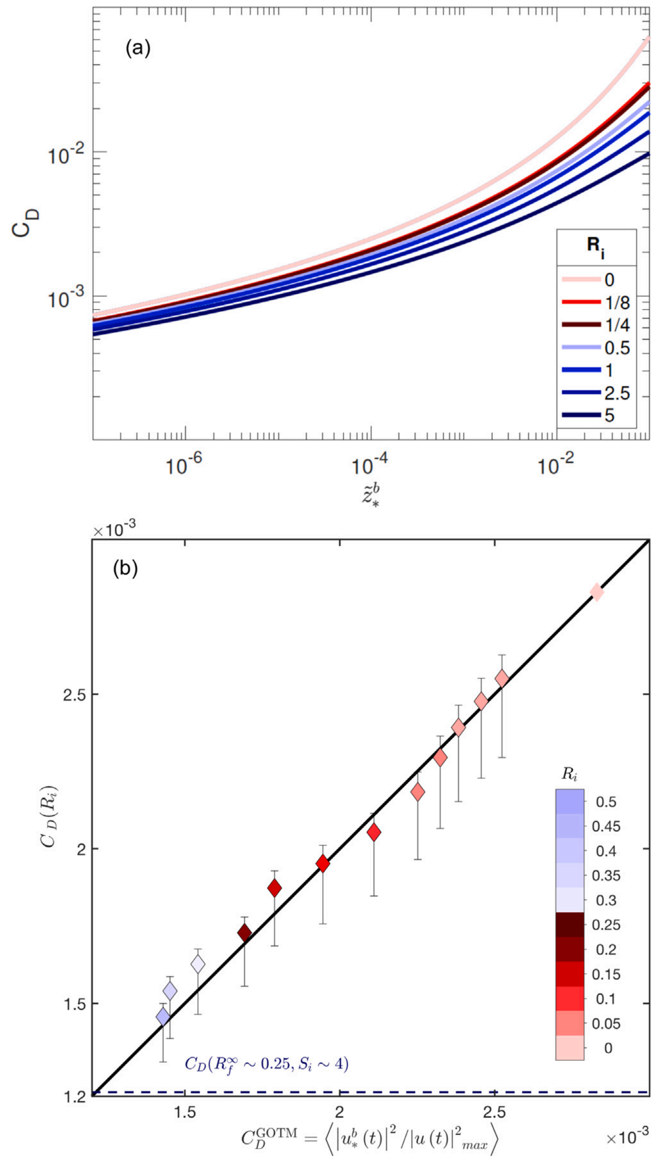

Fig. 2. (a) Bulk drag coefficient C_D as a function of the dimensionless roughness length for varying stratification. (b) Comparison of C_D resulting from GOTM (i.e., using the GOTM output $u_*^b(t)$ and $u(t)$) and Eq. (13) with its lower and upper bounds ($C_0 = 0.9 - 1.03$) shown as error bars. The dashed line corresponds to the lower limit of $C_D(S_i, R_f) = 1 + S_i/R_f$.

increments. The maximum Si^0 (thus the maximum allowable horizontal density gradient) is chosen such that runaway stratification is avoided. Strong near surface stratification is prevented by applying a small wind stress of 0.01027 N m^{-2}.

3.2. Bulk drag coefficient

From a practical point of view, the tidal current amplitude U_T is easier to observe than u_*^b (Simpson et al., 1990). Because stratification varies above the lower part of the boundary layer that is well-mixed in (7), a stratification dependent C_D is needed to reflect the associated deviation from the law of the wall. In (10), the eddy viscosity scale for stratified conditions is defined through the change in l. The same scaling can be written in terms of a stratified friction velocity such that $u_*^b/(u_*^b)_{\text{stratified}} = f\left(R_i\right) = C_0(1 + \kappa\sqrt{R_i/c_b})$. In the limit of weak stratification $R_i \to 0$, $f(R_i) = 1$. For large stable stratification $R_i \to 5$ ($h_b = H/4$), $f(R_i) \approx 1.77$. Hence, the scaling introduced by Burchard et al. (2011) is extended to account for both well-mixed and stratified conditions with $f(R_i)$.

$$C_D = \left[\frac{\kappa/f\left(R_i\right)}{\left(\frac{z_0^b}{H}+1\right)\ln\left(\frac{H}{z_0^b}+1\right)-1}\right]^2 = \left[\frac{(u_*^b)_{\text{stratified}}}{U_T}\right]^2. \tag{13}$$

When the water column is well mixed, (13) reduces to the formulation derived by Burchard et al. (2011). The value of C_D decreases with increasing stratification as shown for a range of scaled z_0^b in Fig. 2a.

The C_D resulting from GOTM runs C_D^{GOTM} is computed by means of a tidally averaged ratio of the model output i.e., bottom friction velocity to maximum depth averaged tidal amplitude and compared to (13) in Fig. 2b. The model results are in good agreement with (13).

The reduction function $f(R_i)$ is analogous to the relation $1 + \gamma S_i$ (Geyer and MacCready, 2014), which is based on a factor that depends on S_i and controls the mixed layer deepening. The upper limit for the ratio of the efficiency of straining to the efficiency of vertical mixing γ is set as $1/R_f^c$ with the critical flux Richardson number $R_f^c = 0.2$ (Ralston et al., 2008). For flows with significant stratification the lower limit of γ is set to $1/R_f^\infty$ with $R_f^\infty = 0.25$ (Venayagamoorthy and Koseff, 2016). Also shown in Fig. 2b as a dashed line, is the bulk drag coefficient corresponding to the upper limit of S_i which will be discussed next.

3.3. Relating S_i to R_i

In (8), vertical density stratification is related to the boundary layer thickness. Ralston et al. (2008) derived a S_i-dependent formulation for h_b ($= H\sqrt{R_f^C/S_i}$) with the critical flux Richardson number $R_f^C = 0.2$ assuming that tidal straining balances turbulent stress divergence at $z = h_b - H$ and adopting log-layer scaling for the shear. This suggests permanent stratification for $S_i > 0.2$, consistent with the model results of Burchard et al. (2011). However, as discussed in Geyer and MacCready (2014) the log-layer scaling for shear may not be valid for flows with significant stratification. These two relations for h_b can be used to write S_i as a function of R_i for the whole range of S_i including the conditions with permanent stratification i.e., $S_i > 0.2$. Two questions then arise: what is the minimum h_b under maximum allowable vertical stratification? What is the S_i associated with such maximum allowable vertical stratification? In (8) the constraints $R_i = 5$ and $h_b = H/4$ are specified based on field observations. In the next section, results from a laboratory experiment and numerical models (DNS and GOTM) are used to test the validity of these constraints, in the context of mixing efficiency for stably stratified flows.

3.3.1. Upper limits for S_i and R_i

Garanaik and Venayagamoorthy (2019) analyzed the results from recent DNS studies on stably stratified flows (Shih et al., 2005; Maffioli et al., 2016) and concluded that mixing efficiency $\Gamma = R_f/(1 - R_f)$ scales with the turbulent Froude number $R_i = F_r^{-2}$ and that in strongly stratified regimes i.e., $F_r < O(1)$, $\Gamma \to 1/3$ while $R_f^\infty = 0.25$. In Fig. 3a, the DNS results are shown in terms of R_i rather than F_r, along with the results of GOTM runs and a lab experiment on mixing in stratified two-layer shear flow (Strang and Fernando, 2001). Due to the limitation of runaway stratification in GOTM, the tidal depth-mean R_i reaches only up to 2. On the other hand, the lab experiment by Strang and Fernando (2001) points to a maximum mixing efficiency of $\Gamma = 1/3$ at $R_i = 5$ owing to the interfacial shear production and eddy transport of mixed–layer fluid entraining to the upper layer, balance each other. This agrees well with the DNS results. With (8) $R_i = 5$ results in $h_b = H/4$; one can then use the relation by Ralston et al. (2008) with the modified flux Richardson number to find an upper limit for S_i such that $\sqrt{R_f^\infty/S_i} = 0.25$ yields $S_i = 4$. This upper limit for S_i is consistent with the observations of Stacey et al. (2001).

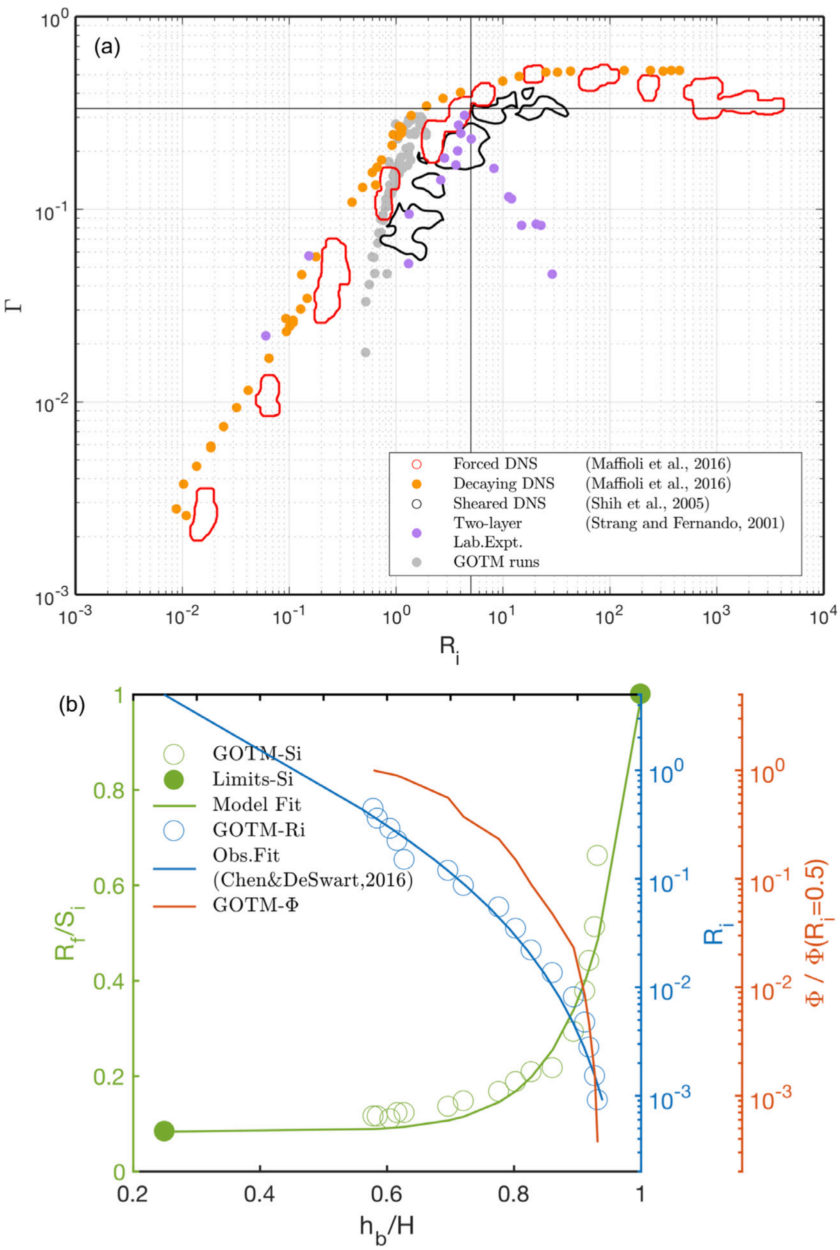

Fig. 3. (a) Mixing efficiency Γ as a function of bulk Richardson number R_i; $\Gamma^{\infty} = 1/3(R_f^{\infty} = 1/4)$ and $R_i = 5$ are marked as black lines. (b) Model-parameterization/observation comparison for R_f/S_i, R_i, and scaled potential energy anomaly ϕ vs. boundary layer thickness h_b.

3.3.2. GOTM fit: R_i and S_i as a function of h_b

First, to test the validity of (8), the GOTM runs are utilized. The results are shown in Fig. 3b. The tidally averaged bulk Richardson number R_i (blue vertical axis) is computed using the density and current output; h_b is computed based on the local maximum in the tidally averaged A_v profile (shown as blue circles). The model results are in good agreement with (8) (Fig. 3b). The accuracy of the tidally averaged R_i calculation from the GOTM output is evaluated by investigating the trend of the scaled potential energy anomaly ϕ (orange vertical axis). Both approaches for depth averaged vertical stratification show similar exponential trends with regard to h_b.

Second, the GOTM runs are used to derive a new relation between R_f/S_i and h_b. Because the maximum S_i that GOTM allows is restricted by runaway stratification, the upper bound is set by the analytical expression derived earlier. For fully-mixed conditions, $R_f = R_f^C$ and the maximum boundary layer thickness equals the water depth H. With these two limits along with the GOTM output, a relation is obtained for a wide range of S_i (green line in Fig. 3b).

$$R_f/S_i = b_0 exp\left[b_1 h_b/H\right] + b_2. \tag{14}$$

In (14) $b_0 = 5.76 \times 10^{-6}$, $b_1 = 12$, and $b_2 = 0.0625$; R_f can be written as a function of Γ.

$$R_f = \Gamma/(1+\Gamma). \tag{15}$$

Given R_i, Γ can be found with Fig. 3a yielding R_f via (15); h_b is obtained via (8). Using R_f and h_b (14) is solved for S_i (Appendix B).

3.4. A_v profile comparison

Finally, tidally averaged A_v^T profiles of GOTM output are used to explore how well the parameterization (7) performs (Fig. 4, left panel). The A_v profiles resulting from the GOTM runs and (7) are in good agreement. The discrepancies may be explained by the fact that (7) does not take into account the direct-wind induced mixing.

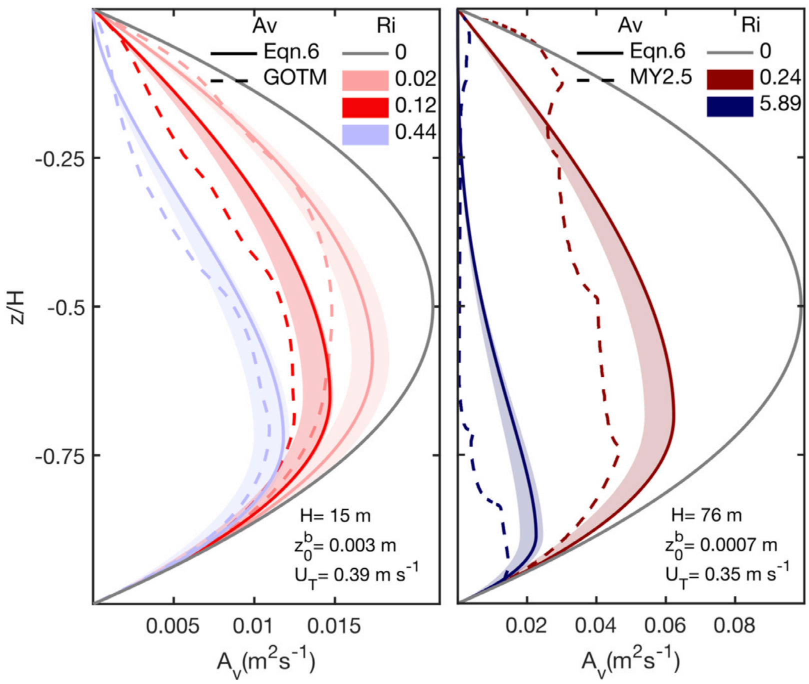

Fig. 4. A_v profiles for various R_i: Comparison of Eq. (7) (bounded solid lines) to numerical model results (dashed lines); GOTM (left panel) and MY2.5 (right panel, Werner et al. (2003)). The lower and upper bounds (shaded area) are based on Eqs. (13) and (14), $C_0 = 0.9 - 1.03$.

Additionally, (7) is compared to the 3D model results of Werner et al. (2003) based on the observations of the tidally driven bottom boundary layer during nearly homogeneous ($N^2 < 10^{-5}$ s^{-2}) and strongly stratified ($N^2 \sim 10^{-4}$ s^{-2}) conditions (Fig. 4, right panel; R_i is calculated based on observed $U_T = 0.35$ m s^{-1} and $H = 76$ m). They used Mellor–Yamada level 2.5 closure (MY2.5) and compared the model results to observations with the a priori specification of density by deriving a time series of density distribution such that vertical stratification matched N^2 estimates from data later to be interpolated on the model grid. Although the boundary layer thicknesses and the local maxima are consistent, the parameterized A_v^T profiles deviate from the model results away from the bed ($z > z_m$) owing to the absence of wind–entrainment effect in (7). The A_v^T comparison shows the capability of (7) in capturing the bottom boundary layer mixing coefficient for a wide range of stratifications. Overall the A_v^T estimates show more consistency with the GOTM-A_v profiles. A flowchart describing the relation between R_i and the eddy viscosity profile and S_i is given in Appendix B.

4. Analytical solution

Using the surface boundary condition (2) and the parameterized eddy viscosity of profile (7), (1) can be solved for u_z:

$$\partial_z u = \frac{z^2 \partial_x B}{2A_v^T} + \frac{z P_x}{\rho_0 A_v^T} + \frac{u_*^s |u_*^s|}{A_v^T}. \tag{16}$$

By integrating (16) over depth an expression for u can be obtained.

4.1. Dimensionless form of the momentum balance

The terms in (16) can be scaled using u_*^b, H and the local Wedderburn number W (Purkiani et al., 2016), resulting in the following non-dimensional variables:

$$W = \frac{u_*^s |u_*^s|}{H^2 \partial_x B} \quad \Leftrightarrow \quad W \cdot S_i = \frac{u_*^s |u_*^s|}{\left(u_*^b\right)^2} \quad , \tag{17a}$$

$$\tilde{z}_0^b = \frac{z_0^b}{H} \quad , \quad \tilde{z}_0^s = \frac{z_0^s}{H} \quad , \quad \tilde{u} = \frac{u}{|u_*^b|} \quad ,$$
$$\tilde{u}_r = \frac{u_r}{|u_*^b|} \quad , \quad \tilde{A}_v^T = \frac{A_v^T}{|u_*^b|\, H} \quad , \quad \tilde{P}_x = \frac{P_x}{\rho_0 \left(u_*^b\right)^2 / H} \quad . \tag{17b}$$

Using these parameters the dimensionless form of (16) is given by:

$$\partial_{\tilde{z}} \tilde{u} = \frac{S_i}{2} \frac{\tilde{z}^2}{\tilde{A}_v^T} + \tilde{P}_x \frac{\tilde{z}}{\tilde{A}_v^T} + W \cdot S_i \frac{1}{\tilde{A}_v^T} \quad . \tag{18}$$

Writing $\tilde{P}_x$ in terms of $\tilde{u}_r$, and using the no-slip boundary condition, $\tilde{u}$ can be expressed as

$$\tilde{u}(\tilde{z}) = \tilde{U}_g + \tilde{U}_w + \tilde{U}_r = \frac{S_i}{2}\gamma_g + W \cdot S_i \gamma_w + \tilde{u}_r \gamma_r, \tag{19}$$

with $\tilde{U}_g$, $\tilde{U}_w$, and $\tilde{U}_r$ denoting the density-driven, wind-driven and residual flow components, respectively; the various γ's are shape functions of the velocity profiles associated with each component (Appendix C).

4.2. Explicit solution

When the surface stress is assumed to be zero ($|u_*^s| = 0$), an explicit solution of (19) exists for $-1 \le \tilde{z} \le \tilde{z}_*$ with $\tilde{z}_* \approx -\tilde{z}_0^s$. The piecewise solution is composed of a Gauss-hypergeometric function, $\tilde{\mathcal{F}}_{2,1}$, and a logarithmic function for the upper and the lower layer, respectively. Explicit solutions for the upper layer are restricted to non-integer α, and are given in Appendix D. Although implicit solutions exist for integer values of α, it is not shown in Appendix D. Instead, a more general approach that provides solutions for a wider range of α is discussed below.

4.3. Approximation of A_v^T

Analytical solutions to the exchange flow with any eddy viscosity profile are not readily available because the non-integer values of α entails solving Fractional Calculus problems. To obtain solutions for a wider range of $\alpha \in \mathfrak{R}$, a constrained-polynomial fitting approach is adopted for the eddy-viscosity profile in the top layer. This consists of

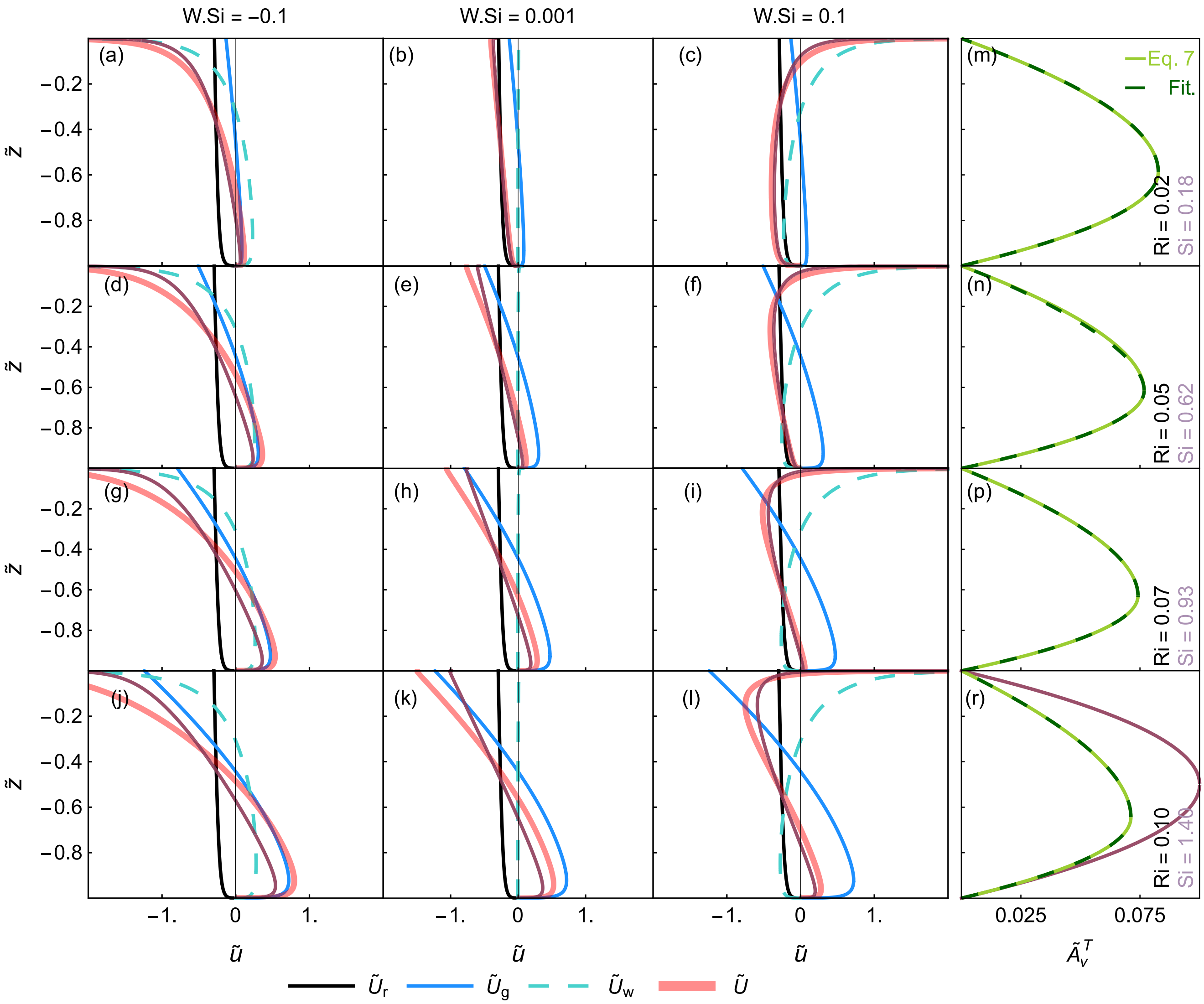

Fig. 5. Composition of non-dimensional exchange flow $\tilde{U}$ for weakly stratified conditions (left panel) under varying S_i and R_i with directional winds i.e., down-estuary winds, $W \cdot S_i < 0$ (first column); up-estuary winds, $W \cdot S_i > 0$ (third column). The $W \cdot S_i$ indicates the ratio of friction velocities (Eq. (16)a). The A_v profile is approximated with the polynomial transformation (right panel) with the corresponding R_i (black font) and S_i (gray font) labels. The relevant parameters are chosen as: H = 10 m, z_0^b = 1.5 10^{-3} m, z_0^s = 1.5 10^{-5} m, $\tilde{u}_r = -0.25$, U_n = 0.03 . The dark red line denotes exchange flow $\tilde{U}$ resulting from parabolic A_v profile as referenced in (r) with same color.

finding the coefficients of a polynomial of degree n, that is the best fit to the profiles resulting from (7) in a least-squares sense with constraints satisfying the value and the gradient near the surface and at $\tilde{z} = \tilde{z}_m$, respectively .

$$A_v^{T_U} \approx p_n \tilde{z}^n + p_{n-1} \tilde{z}^{n-1} + \cdots + p_1 \tilde{z} + p_0, \tag{20}$$

with $p_0 \ldots p_n$ being the polynomial coefficients. The approximation is detailed in Appendix C.

The solution is obtained within $\tilde{z}_m \le \tilde{z} \le \tilde{z}_*$ where $\tilde{z}_* \approx -\tilde{z}_0^s$ ($\tilde{z}_* = 0$) is associated with $u_*^s = 0$ ($u_*^s \neq 0$) (Appendix D, D3-4). With $u_*^s = 0$ and $A_v^{T_U}(z = 0) = 0$, one of the roots of (20) is equal to zero resulting in an undefined solution (D4). Therefore, for $u_*^s = 0$ an upper limit of $\tilde{z} = -\tilde{z}_0^s$ is used when calculating $A_v^{T_U}$. This solution seamlessly attaches to the $A_v^{T_L}$ at $\tilde{z} = \tilde{z}_m$ given in (3).

5. Exploration of the parameter space

The velocity profiles are analyzed based on the dimensionless parameters R_i and $S_i \cdot W$. To quantify the strength of the exchange flow, a definition introduced by Burchard et al. (2011) is used. Here, it is modified to satisfy the change in boundary layer thickness and is expressed for one-dimensional cases as:

$$\tilde{M} = 4 \int_{-1}^{0} \tilde{u}(\tilde{z}) \left(\tilde{z} + \frac{h_b}{2H} \right) d\tilde{z}, \tag{21}$$

which is the dimensionless exchange intensity that considers the orientation of the near-bed currents. For a step-like exchange flow with a value of $\tilde{u} = 1$ ($\tilde{u} = -1$) at depths $\tilde{z} < \tilde{z}_m$ ($\tilde{z} > \tilde{z}_m$), (21) results in −1. Values of $\tilde{M} < 0$ ($\tilde{M} > 0$) stands for classical (inverse) circulation.

Sensitivity of the exchange flow to $W \cdot S_i$, R_i (parabolic vs. non-parabolic A_v profiles), $\tilde{u}_r$, and $\tilde{z}_0^s$ (constant vs. wind−stress dependent) is explored (Table 1). The default parameter values are H = 10 m, $\tilde{z}_o^b = 1.5 \cdot 10^{-4}$, and the unsteadiness number, $U_N = \omega H / u_*^b$, defined as a proxy for the scaled frequency (Burchard and Hetland, 2010) with $\omega = 2\pi/T$. Given a characteristic value for U_N, and a tidal period T = 12.4 hr as the dominant tidal constituent, one can obtain the friction velocity scale and tidal current amplitude using C_D, obtained from (13).

The base case consists of $\tilde{z}_0^s = 1.5 \cdot 10^{-6}$, $\tilde{u}_r = -0.25$, with varying R_i and $W \cdot S_i$. For the second set of experiments, R_i is kept constant (well-mixed condition). For the next set, $\tilde{u}_r = 0$ is used; for the fourth

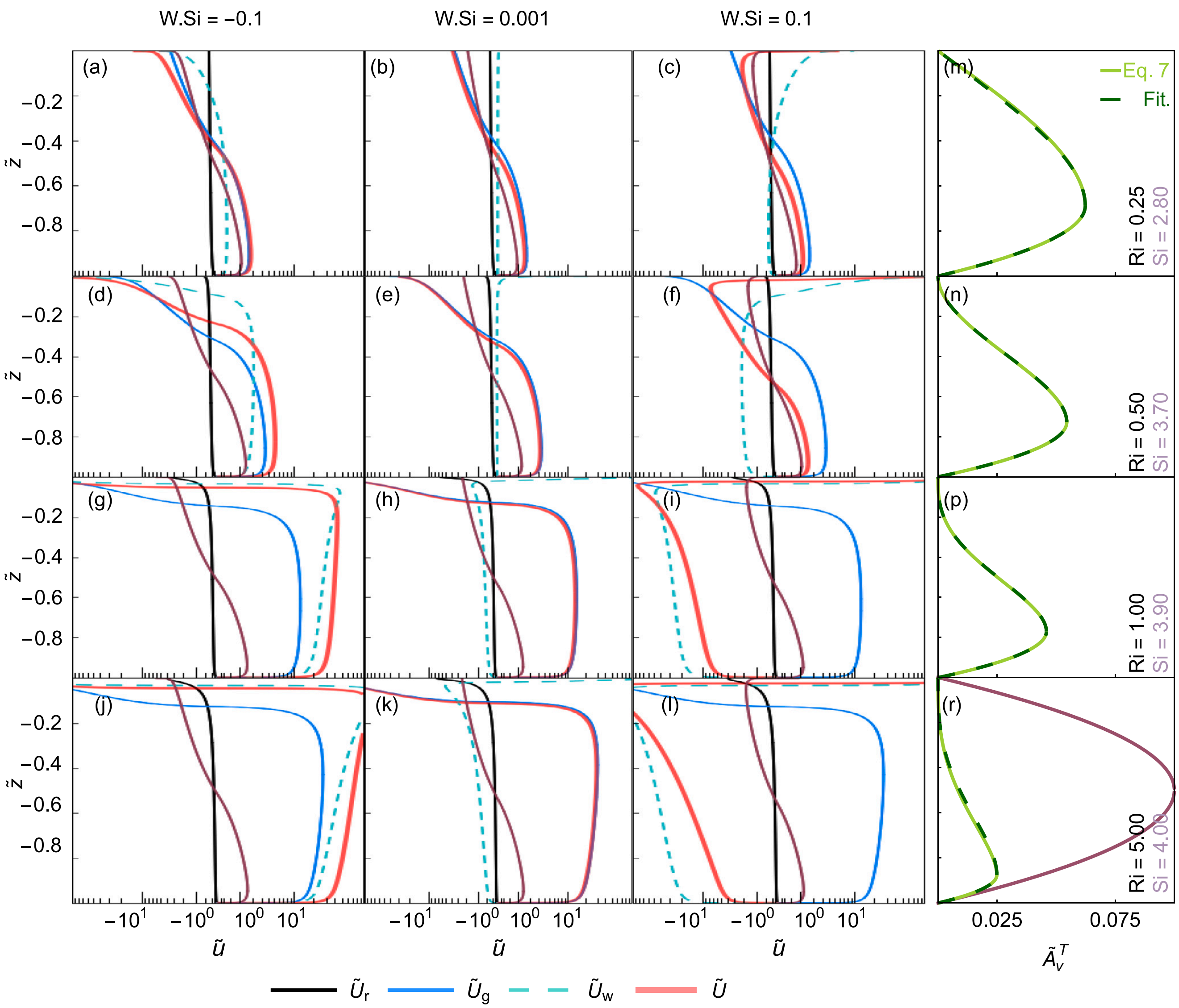

Fig. 6. As in Fig. 5, but for stronger stratification, $R_i \geq 0.25$.

Table 1
Case scenarios with $-2 \leq W \cdot S_i \leq 2$ (increments of 0.1 for $|W \cdot S_i| > 1$ and 0.02 for $|W \cdot S_i| \leq 1$).

Case	R_i	$\tilde{z}_o^s$	$\tilde{u}_r$
1	0.01 – 0.1 with 0.01 increments, 0.1 – 0.25 with 0.025 increments, 0.3, 0.4, 0.5, 1 and 5	$1.5 \cdot 10^{-6}$	−0.25
2	0.001	$1.5 \cdot 10^{-6}$	−0.25
3	0.01 – 0.1 with 0.01 increments, 0.1 – 0.25 with 0.025 increments, 0.3, 0.4, 0.5, 1 and 5	$1.5 \cdot 10^{-6}$	0.00
4	0.01 – 0.1 with 0.01 increments, 0.1 – 0.25 with 0.025 increments, 0.3, 0.4, 0.5, 1 and 5	$a_c\left(u_*^s\right)^2/gH$	−0.25

set of experiments, the surface roughness length varies with the surface friction velocity as

$$\tilde{z}_0^s = a_c\left(u_*^s\right)^2/gH\ , \tag{22}$$

with $a_c = 1400$ (Charnock, 1955; Craig and Banner, 1994).

5.1. Composition of the exchange flow profile

The subtidal flow profiles for the first set of experiments (i.e., $W \cdot S_i$ and R_i are varied; $W \cdot S_i > 0$ denote up-estuary winds and $W \cdot S_i < 0$ denote down-estuary winds) show change in shape and strength (Figs. 5 and 6 with relatively weak and strong stratification). Down-estuary

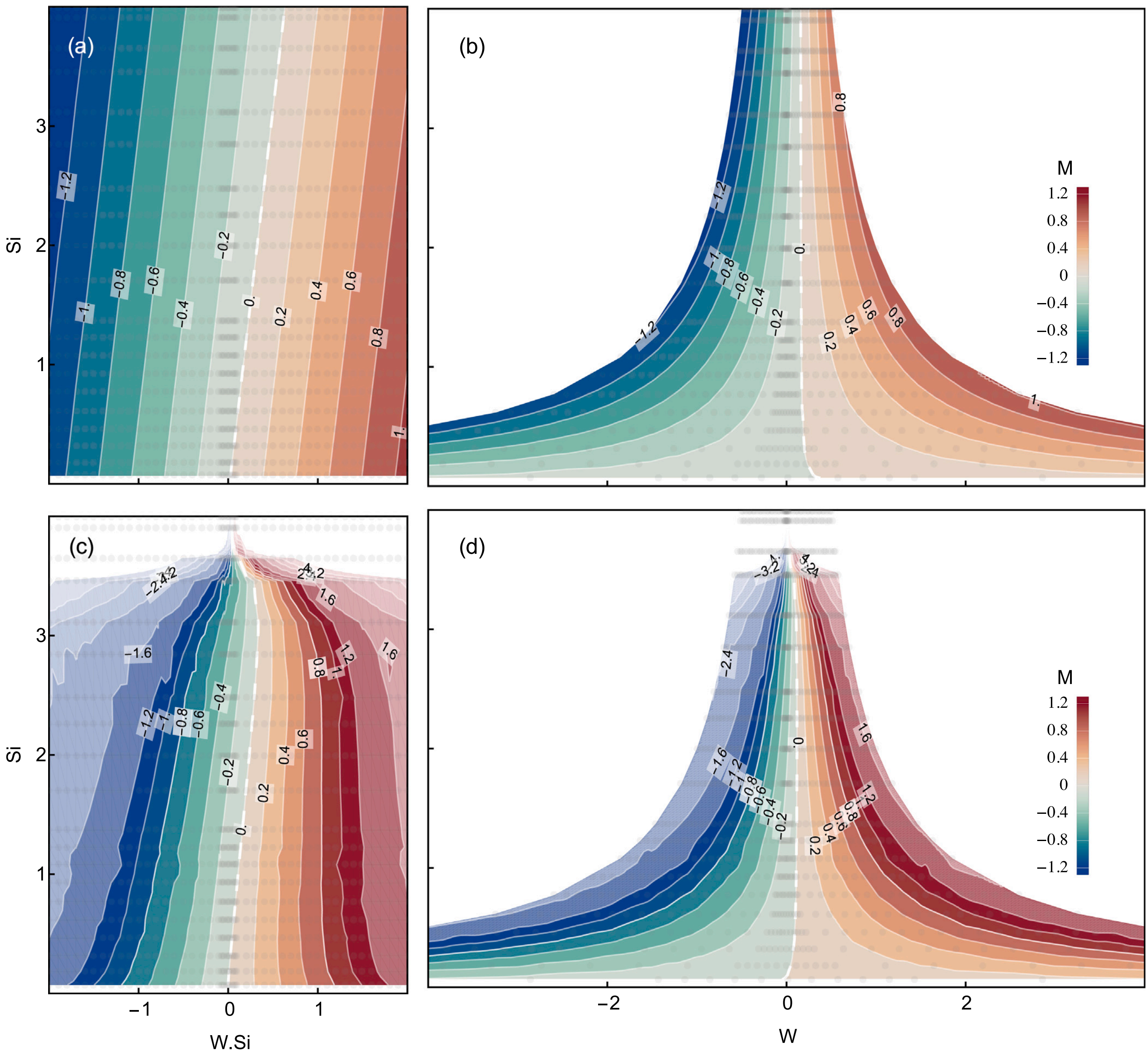

Fig. 7. Estuarine exchange strength $\tilde{M}$ for varying S_i, R_i, $W.S_i$ and W (up-estuary, $W \cdot S_i > 0$; down-estuary, $W \cdot S_i < 0$; $W \cdot S_i$ indicates the ratio of friction velocities, Eq. (16)a). Classical and inverted estuarine circulation are associated with $\tilde{M} < 0$ and $\tilde{M} > 0$, respectively. $\tilde{M}$ is calculated for A_v profiles (a, b) that are parabolic, i.e., $R_i = 0$ while S_i varies (Case #2, Table 1), (c, d) resulting from R_i-S_i co-dependence as shown in Figs. 5 & 6 (Case #1, Table 1) . Other parameters are same as in Figs. 5 & 6. The contours are based on an interpolation over data points (gray dots); $\tilde{M} = 0$ is shown as a white dashed line; beyond the colormap limits the colors fade to white as the order of magnitude of $\tilde{M}$ reaches 2 (c, d).

wind enhances the classical circulation driven by gravitational circulation with up-estuary flow near the bottom and down-estuary flow near the surface. Up-estuary wind on the other hand results in more complicated flow profiles with either a two-layer inverted circulation, or a three-layer flow that is up-estuarine at the surface with classical two-layer circulation underneath (Figs. 5 and 6, third column).

For relatively weak stratification (Fig. 5a) down-estuary wind promotes a weak return flow. For stronger stratification (Fig. 5d, g, j), both the down-estuary wind induced return flow and gravitational circulation increase in strength. The velocity profiles under up-estuary winds are more sensitive to stratification. The interplay between gravitational forcing and up-estuarine wind results in an enhanced up-estuarine near surface flow with an enhanced down-estuarine flow underneath ($-0.6 \le \tilde{z} \le 0$, Fig. 5i,l). For up-estuarine winds with relatively strong stratification (Fig. 6), the down-estuary component of gravitational circulation is restricted to a small layer of the water column near the surface. This is due to the decreasing boundary layer thickness, resulting in a shape of A_v profile that strongly deviates from parabolic (Figs. 5 and 6, right panel) and leads to enhanced subtidal flows.

Another striking point with up-estuarine wind is the condition that sets the number of flow layers (two-layer or three-layer flows). Both the R_i number and the magnitude of the prescribed residual runoff flow ($\tilde{u}_r = -0.25$) play an important role in exciting an inverted two-layer circulation (Fig. 5c,f $R_i = 0.02, 0.05$; Fig. 6i,l $R_i = 1.00, 5.00$). When the density driven flow cancels out the up-estuarine wind driven flow, the residual flow $\tilde{u}_r$ direction determines $\tilde{u}$ at $-1 \le \tilde{z} \le -0.2$ (Fig. 5f, $R_i = 0.05$). Inverted circulation is found when up-estuarine wind driven flow exceeds the density driven flow in magnitude (e.g., Fig. 6i,l

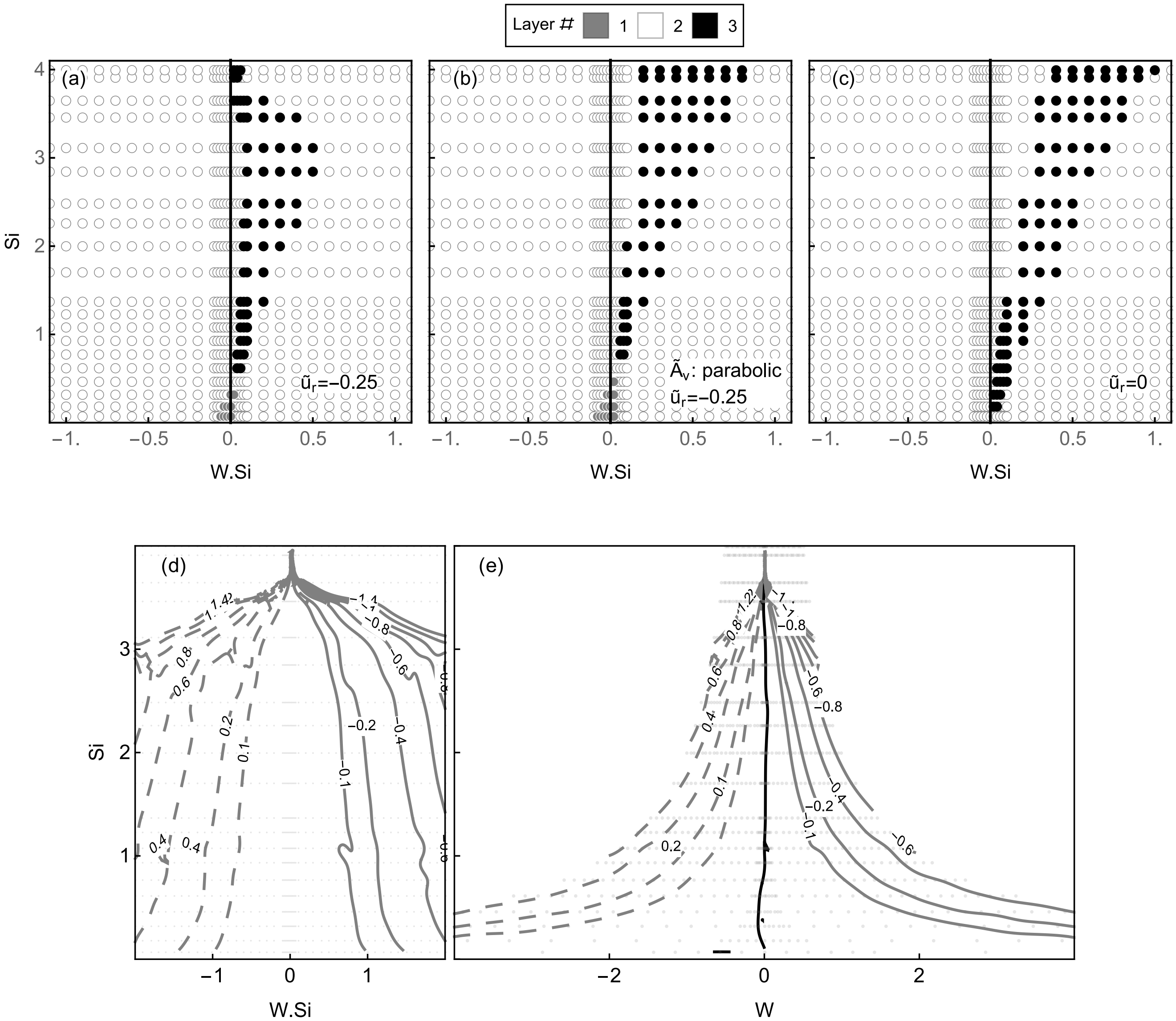

Fig. 8. (a, b, c) Number of velocity layers of Case #1, #2, and #3 Table 1. (d, e) The difference in estuarine exchange intensity ΔM due to varying z_0^s; ΔM is calculated by subtracting the intensity associated with the constant $z_0^s = 1.5\ 10^{-5}$ m (Case #1, Table 1) from the intensity associated with τ−dependent z_0^s (Case #4, Table 1).

$R_i = 1.00, 5.00$). Thus, the emergence of inverted circulation depends on different conditions: one relatively well-mixed water column and weak baroclinic pressure gradient (Fig. 5c,f), the other totally dominated by wind-driven flow (Fig. 6i,l).

The exchange flow profiles $\tilde{U}$ with parabolic eddy viscosity profiles (Case 2, Table 1) are shown in Figs. 5 and 6 (dark red lines) for comparison. This case consists of a fixed R_i, thus S_i varies independent of R_i. When compared to the exchange flow profiles with R_i- dependency the solution with parabolic eddy viscosity profiles underpredict the intensity of the circulation under both up-estuary and down-estuary winds. The difference will be analyzed further in the context of exchange flow intensity in the following section.

5.2. Exchange flow intensity

Following Lange and Burchard (2019), the exchange flow intensity $\tilde{M}$, defined in (21), is analyzed as a function of the dimensionless parameters: S_i, W, and $W \cdot S_i$ (Fig. 7). The type of estuarine circulation (classical $\tilde{M} < 0$; inverted $\tilde{M} > 0$, respectively) is associated with wind direction (down-estuary $W \cdot S_i < 0$; up-estuary $W \cdot S_i > 0$). Purely density driven circulation corresponds to $W = 0$. The slight shift of the $\tilde{M} = 0$ isoline in the upstream direction is associated with the run-off velocity $\tilde{u}_r$, see the $\tilde{M} = 0$ isoline in both the $S_i - W$ and $S_i - W \cdot S_i$ domains.

When the influence of vertical stratification is included (Fig. 7c, d), the flows get stronger and the exchange flow intensity $\tilde{M}$ increases twice within $|W \cdot S_i| < 1$. The slope of the $\tilde{M}$ isolines increases with S_i and changes sign with wind direction, that is positive (negative) for down-estuary (up-estuary) winds (Fig. 7c). For $S_i > 3.5$ the order of magnitude of $\tilde{M}$ reaches 2 with the significant increase of $\tilde{U}$ at the surface (Fig. 6f-l). The significant increase in exchange flow, shown as a white area with gray dots (Fig. 7c, d), is associated with the neglect of wind entrainment and surface mixed layer development in the eddy viscosity parameterization (7). The strong shear in Fig. 6f–l is related with underestimation of near-surface eddy viscosity. Hence, the white-gray-dotted area marks the limitation of the model such that for $S_i > 3.5$ the applicability of the model is constrained to relatively weak wind stress e.g., $|W \cdot S_i| \lesssim 0.1$. Because the adjustment of stratification

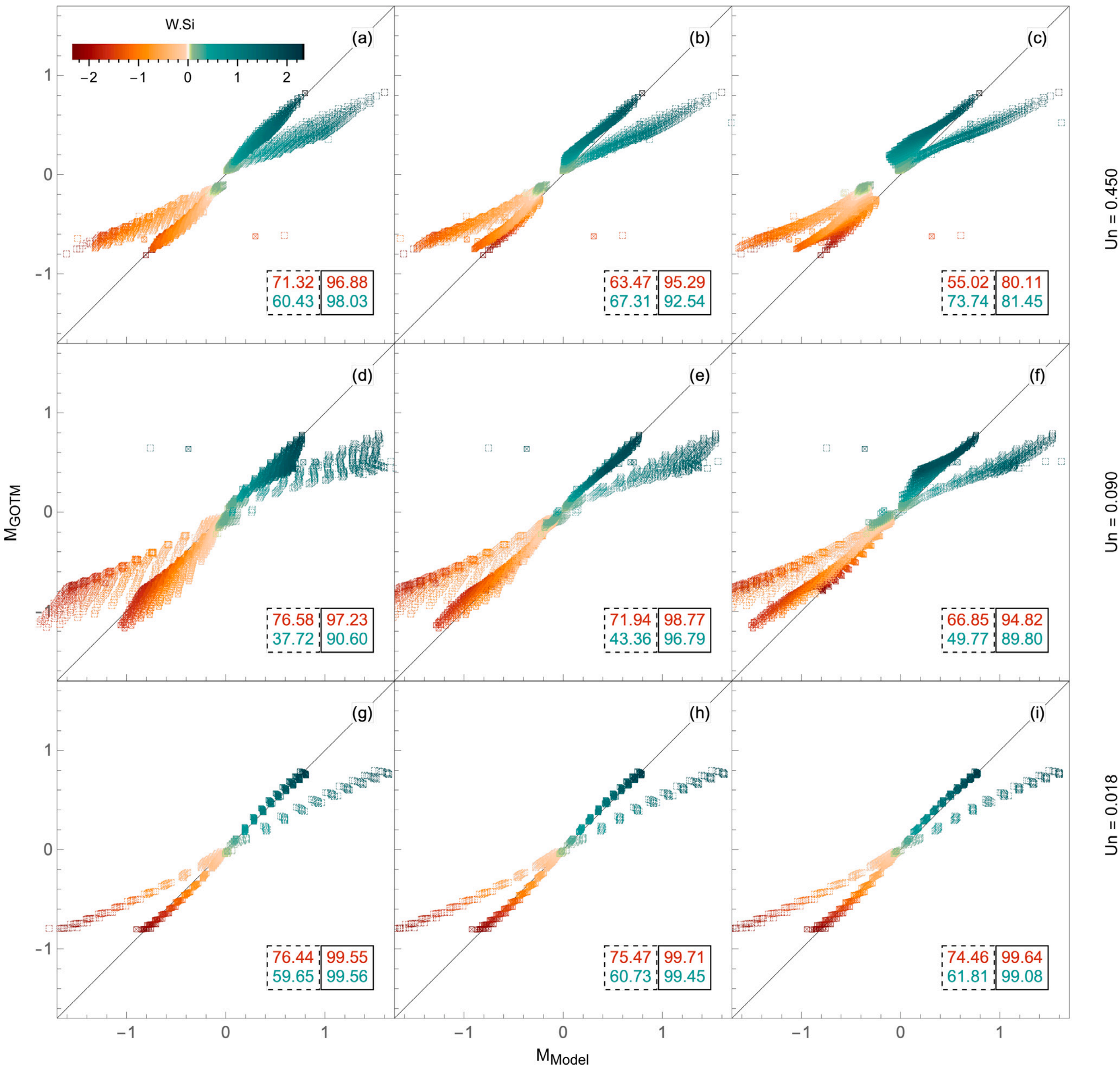

Fig. 9. Exchange flow intensity comparison M_{MODEL} vs. M_{GOTM} with $\tilde{u}_r = 0$, $H = 10$ m, and $U_N = 0.018$, 0.09, and 0.45 (corresponding to tidal current amplitudes of $U_T = 1.50$, 0.30, and 0.06 m s^{-1}). M_{MODEL} is calculated by modifying the relative contributions of gravitational and wind driven components of the exchange flow: $\tilde{U}_g$ (a, d, g) , $2\tilde{U}_g$ (b, e, h), and $3\tilde{U}_g$ (c, f, i) . Crossed and dotted markers denote wind driven contributions of $\tilde{U}_w$ and $1/2\tilde{U}_w$. Skill coefficient (as %) for upestuarine/downestuarine winds is shown in green/red colors at the bottom corner with dotted/solid frame indicating wind driven contributions of $\tilde{U}_w$ and $1/2\tilde{U}_w$. (For interpretation of the references to color in this figure legend, the reader is referred to the web version of this article.)

due to wind is ignored in A_v^T, the applicability of the model can be further constrained to $|W \cdot S_i| < 1$ (surface stresses smaller than bottom stresses) for $S_i < 3.5$.

Additionally, the parameter space can be explored in terms of the number of velocity layers, which give insight in the change of the flow profiles. The number of velocity layers is determined based on how many times the exchange flow changes direction. This is shown in Fig. 8 where the colors gray, white, black correspond to a single layer, a two and a three layer solution, respectively.

The region in parameter space where a 3-layer flow exists is smaller if non-parabolic eddy viscosity profiles are considered (Case 1 Fig. 8a) compared to the parabolic ones (Case 2, Fig. 8b); these conditions are found for $0 < W \cdot S_i < 0.5$. The exchange flow structure also depends on the magnitude of $\tilde{u}_r$. For relatively small runoff velocity, $\tilde{u}_r = -0.25$, a single-layer flow exists only for the weak winds and $S_i < 0.5$ (Fig. 8a, b). However, for no-runoff case $\tilde{u}_r = 0$, single-layer flow does not develop; a 3-layer flow exists even when $S_i < 0.5$ (Fig. 8c).

5.3. The surface roughness

The length scale for the surface roughness plays an important role in the intensity of the exchange flow as it changes the flow velocity at the surface. This is investigated with the set of analytical solutions where the influence of variations in $\tilde{z}_0^s$ on the exchange flow structure are shown as the difference between the two cases i.e., with a τ dependent $\tilde{z}_0^s$ (Case #4) and a prescribed one (Case #1) (Fig. 8d,e). The exchange flow intensity increases with τ dependent $\tilde{z}_0^s$ (Fig. 8d, e). The exchange flow intensity increases due to higher velocities at the surface originating from a very small $A_v^T(z=0) = \kappa \left|u_*^s\right| z_0^s$. With the τ dependent $\tilde{z}_0^s$, eddy viscosity at the surface becomes proportional to $\left|u_*^s\right|^3$.

5.4. Modifications to $\tilde{u}$

One drawback of the analytical solution is that the tidal variations in eddy viscosity profile is ignored yielding underestimations in the exchange flow as a result of the absence of ESCO-generated circulation. Dijkstra et al. (2017) identified tidal and gravitational ESCO circulations as distinct physical mechanisms contributing as much as gravitational circulation with relative contributions of 1/3 each in a well-mixed or partially stratified estuaries. To evaluate the accuracy of the exchange flow (19), tidally averaged GOTM current profiles are used with varying unsteadiness number U_N(=0.018, 0.9, 0.45), prescribed S_i^0(= 0.01 to 0.1 with 0.01 increments; 0.1 to 1 with 0.025 increments) and $(W \cdot S_i)^0$(= −1 to 1 with 0.1 increments; −0.1 to 0.1 with 0.02 increments).

Analytical model results (19) are in good agreement with GOTM only for relatively small $|W.Si|$ (dotted markers in Fig. 9a,d,g; see Fig. 10a, b). The discrepancies arise with increasing magnitudes of $|W.Si|$ yielding overestimates/underestimates with downestuarine/upestuarine winds. The discrepancy arises because GOTM adjusts the bottom stress based on the prescribed wind stress (i.e., friction velocity ratio is updated during the simulation). This entails modifying the wind driven component $\tilde{U}_w$ in (19); approximated as $1/2\tilde{U}_w$ to account for the wind-driven increase in bottom stress. Although wind driven change in bottom stress depends on stratification adjustment and directional-wind induced entrainment which is excluded in this study, the approximation improves the correlation significantly (crossed markers in Fig. 9a,d,g). The skill assessment of the analytical model is given in Appendix F.

The correlation depends significantly on the unsteadiness number U_N and the associated change in exchange flow generated by ESCO. The exchange flow obtained by (19) is modified by enhancing its gravitational component to account for the ESCO driven flow (second and third columns in Fig. 9). For $U_N = 0.45$ (relatively small tidal current amplitude) the model predicts GOTM output better with U_g suggesting that the ESCO circulation is negligible; for $U_N = 0.09$ the gravitational contribution of $2U_g$ yields a better correlation (Fig. 9a, e; see the exchange profiles in 10c, d) showing that ESCO plays an important role. The GOTM simulations with smaller $U_N = 0.018$ allows for $S_i < 0.3$; with relatively small U_N and S_i the change in gravitational contribution does not affect the correlation between the model and GOTM significantly (Fig. 9 g,h,i) .

The exchange flow intensity shown in Fig. 7c,d is modified to include the wind and density driven changes associated with the intermediate $U_N = 0.09$ (Fig. 11). The $\tilde{M} \le 0$ isolines shift upestuary allowing for stronger downestuarine exchange flow under relatively small $|W.Si|$ (Fig. 11a,b). With reduction in wind driven contribution due to enhanced bottom stress, the $\tilde{M}$ isolines widen and shift further upstream (Fig. 11c,d). This leads to reduce inverted upestuarine circulation and enhanced 3-layer flow profiles.

6. Discussion

The one-dimensional analytical solution that is based on the new eddy viscosity parameterization provides insights into the composition of exchange flow profiles under varying wind forcing. The parameter space analysis shows a clear increase in the intensity of the exchange flow with the inclusion of vertical stratification. This is associated with decreasing bottom boundary layer thickness, and with eddy viscosity values decaying to relatively insignificant values near the surface.

The parameters explored in this study are S_i, $W \cdot S_i$, $\tilde{u}_r$, and $\tilde{z}_0^s$. Two values for $\tilde{u}_r$ are used to determine the influence of run-off on estuarine circulation (Table 1). A typical value for $\tilde{z}_0^s$ $(= 1.5 \cdot 10^{-6})$ is compared to a parameterization that depends on wind speed, and thus on W. The range for $W \cdot S_i$ is chosen to cover both the cases $\tilde{u}_*^s \ge \tilde{u}_*^b$ and $\tilde{u}_*^s < \tilde{u}_*^b$. The maximum $S_i = 4$ $(R_i = 5)$ is chosen based on the observations (Chen and De Swart, 2016; Stacey et al., 2001). The numerical model results of Li et al. (2008), point out to instantaneous values of $S_i > 3$ throughout the tidal cycle. Although in this study tidally averaged eddy viscosity profiles are used, to explore a wider range of parameters, $S_i = 4$ is chosen to be the upper limit.

With the implementation of a non-zero surface roughness and allowing for stratification, the new solution provides improvements over the solution introduced in Lange and Burchard (2019). The solution presented in this study allows for flexible eddy viscosity profiles that are determined based on dimensionless physical parameters. This offers a substantial improvement over the analytical solution given by Chen and De Swart (2016) which is limited to specific eddy viscosity profiles (i.e., constant, linear, or parabolic upper layer) with shape functions that rely on a numerical model. The novel parameterization can also be used in estimating tidally averaged eddy viscosity profile in observational estuarine studies with weak to moderate wind forcing when turbulent measurements are readily unavailable. This requires simple in situ measurements of CTD to determine the bulk R_i, characteristic tidal amplitude, and wind stress.

The eddy viscosity parameterization offers a simple way to predict subtidal eddy viscosity profiles under weak to moderate wind forcing in partially stratified systems. One of the limitations is that the tidal variations in eddy viscosity is excluded for simplicity. Therefore its contribution to the exchange flow resulting from its covariance with vertical shear is ignored. Another limitation to the parameterization is the absence of surface mixed layer resulting from wind entrainment, that could be addressed in future research.

The scientific approach chosen here, using a constant longitudinal buoyancy gradient $\partial_x B$ has drawbacks as its correlation with advective buoyancy flux and the tidal velocity is ignored. As documented by Burchard et al. (2011) 1D GOTM simulations with constant $\partial_x B$ result in upstream salt fluxes. This is evidenced by 1D buoyancy equation for rectilinear tidal motion subject to $\partial_x B$ that is constant in time and space i.e., $\partial_t B + u(t,z)\partial_x B = \partial_z \left(K_v \partial_z B\right)$ with eddy diffusivity K_v. Under the steady-state assumption, vertically and tidally averaging the buoyancy equation yields $\partial_x B \int_{-H}^{0} \langle u(t,z)\rangle dz = 0$ with no-flux conditions at the surface and bottom and $\langle\rangle$ denoting tidal averages. Because $\partial_x B \ne 0$, the condition of a steady-state solution for buoyancy is inconsistent with a non-zero runoff velocity. Another drawback is that a non-zero residual velocity (total residual flow is the sum of local runoff and exchange flows) does not allow for a steady-state solution. However, this less critical inconsistency can be resolved by using the non-zero term to compensate for the tidal mean of buoyancy deviations such that $\langle \partial_t B\rangle = -\frac{1}{H}\left\langle \int_{-H}^{0} u(t,z)dz \right\rangle \partial_x B$.

The novel technique used in obtaining exchange flow profiles offers a new approach in analytically solving problems that otherwise depend on numerical methods. With constrained–polynomial fitting approach physically–driven eddy viscosity profiles can be approximated precisely. This makes analytical solution possible by avoiding Fractional Calculus problems.

7. Conclusion

The significance of directional and longitudinal wind forcing in contributing to the exchange flow was explored under varying vertical and longitudinal stratification. We developed an eddy viscosity parameterization that takes into account stratification depending on the boundary layer thickness, and the dimensionless numbers i.e., the Simpson number, the Richardson number and the Wedderburn number. The piecewise analytical solution for the exchange flow offers a

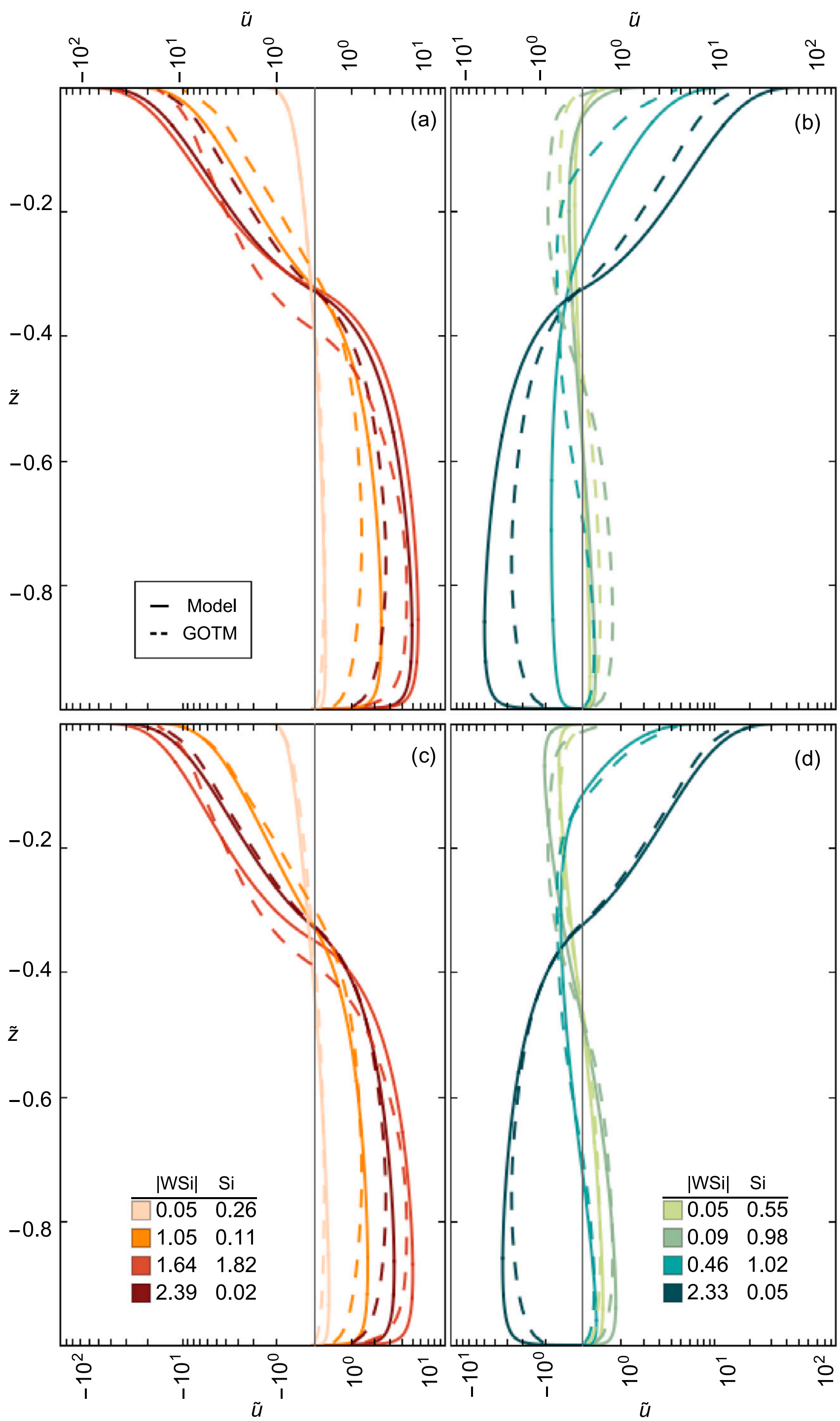

Fig. 10. Dimensionless exchange flow profiles resulting from GOTM (dashed lines) and the analytical model (solid lines) with $\tilde{u}_r = 0$ and $\tilde{U}_N = 0.09$ for (a, c) downestuarine and (b, d) upestuarine winds. Analytical model output in (a, b) and (c, d) is obtained as $\tilde{U}_g + \tilde{U}_w$ and $2\tilde{U}_g + {}^1/_2\tilde{U}_w$, respectively (associated with dotted and crossed markers in Fig. 9d and e) .

simple yet robust way to explore a wide range of relevant dimensionless parameters as the typical runtime is in the order of seconds. Departure from parabolic eddy viscosity profiles with increasing horizontal and vertical stratification, results in an inverted circulation with enhanced down-estuary return flow, under up-estuary winds. Three-layer exchange flow emerges only when bed friction velocity is much smaller than up-estuarine surface friction velocity. Increase in residual runoff flow changes the composition of exchange flow, suppressing the three-layer evolution and promoting inverted flow for even weaker stratification. Single layer formation under down-estuary winds becomes more common for larger Wedderburn number and smaller Simpson number. Exchange flow intensity depends significantly on surface roughness, and leads to larger flows when associated with surface friction velocity.

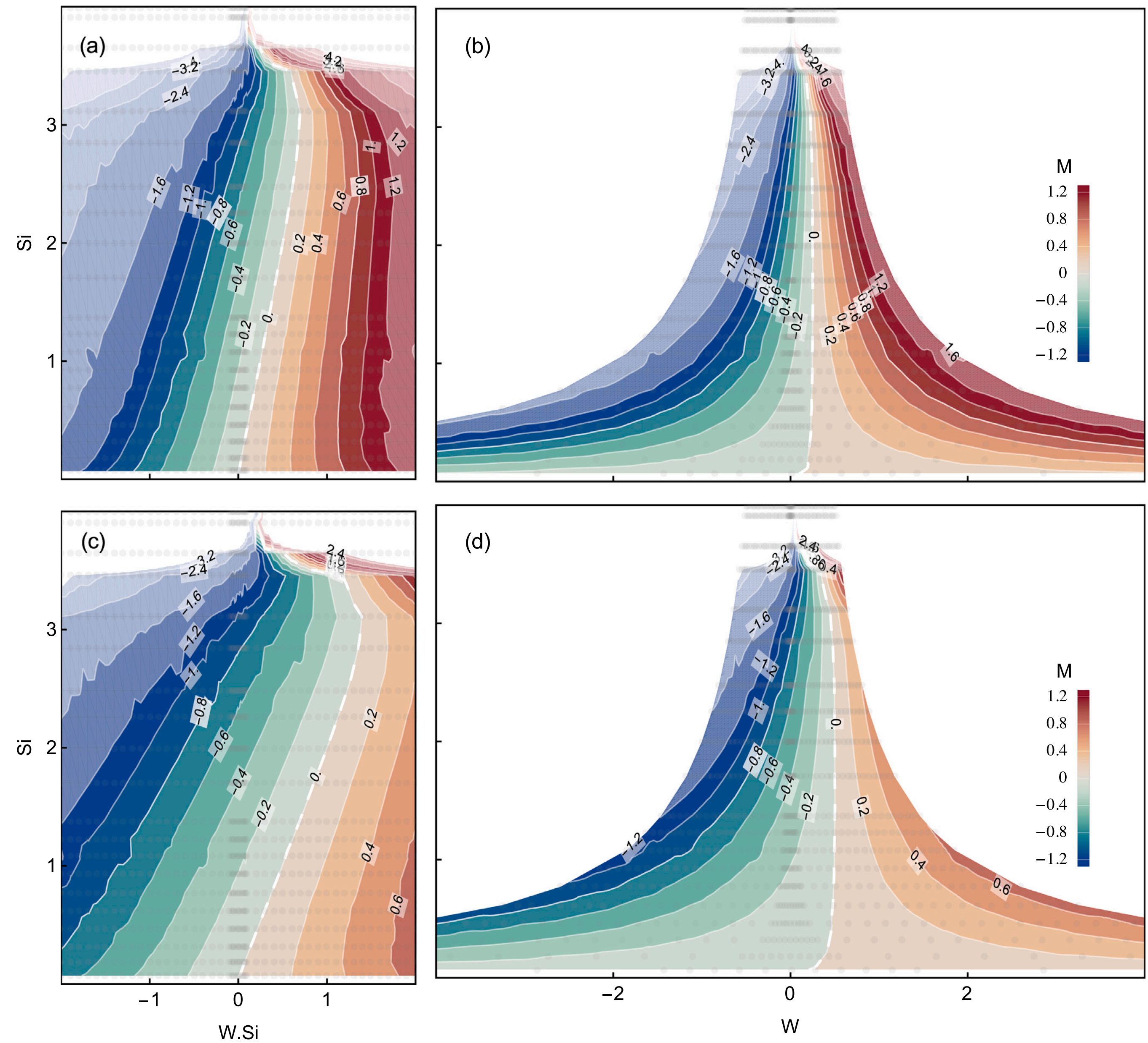

Fig. 11. As in Fig. 7c,d (i.e., A_v profiles with $R_i - S_i$ co-dependence; $\tilde{u}_r = -0.25$) but for exchange flow profiles calculated as (a, b) $2\tilde{U}_g + \tilde{U}_w + \tilde{U}_r$ and (c, d) $2\tilde{U}_g + {}^1/_2\tilde{U}_w + \tilde{U}_r$.

Declaration of competing interest

The authors declare that they have no known competing financial interests or personal relationships that could have appeared to influence the work reported in this paper.

Acknowledgments

We thank two anonymous reviewers for their valuable insights, which helped to improve the manuscript. The work by Hans Burchard has been supported by the Research Training Group 'Baltic TRANSCOAST' funded by the DFG (Deutsche Forschungsgemeinschaft) under grant number GRK 2000/1.

Appendix A. The shape parameter α

Assuming $\kappa \left|u_*^s\right| z_0^s$ is relatively small compared to the rest of the terms in (4) and $h_b \gg z_0^b$, the integration in ((10) & (11)) can be simplified and written in a dimensionless form. Under well mixed conditions $\int_{-1}^{0} \overline{\widetilde{A_v}}\, d\tilde{z} \approx \kappa/6$; for bottom layer under stratified conditions $\int_{-1}^{\tilde{z}_m} \overline{\widetilde{A_v^{T_L}}}\, d\tilde{z} \approx \kappa \tilde{h}_b^2/12$. Using the definition for the probability density function of beta distribution, the top layer of the scaled eddy viscosity is integrated. The left side of (10) yields

$$\left(\frac{1}{6}\right)/\left[\frac{\varsigma^0\left(1-\tilde{h}_b/2\,,\alpha,\beta\right)}{\left(1-\tilde{h}_b/2\right)^{\alpha-1}\left(\tilde{h}_b/2\right)^{\beta-1}}\,\frac{\Gamma(\alpha)\Gamma(\beta)}{\Gamma(\alpha)+\Gamma(\beta)}\,\frac{\tilde{h}_b}{4}+\left(\frac{\tilde{h}_b^2}{12}\right)\right] = \frac{C_0}{\tilde{h}_b}\left(1+\frac{\kappa\sqrt{R_i}}{c_b}\right) \tag{A.1}$$

with $\beta = \tilde{h}_b(\alpha-1)/(2-\tilde{h}_b)+1$, the incomplete beta function ς^0 (defined in terms of hypergeometric functions) and the gamma function Γ; C_0 is a constant. Because α cannot be expressed explicitly as a function of R_i from (A.1), the relation (12) is derived by fitting a function for α that satisfies both sides of (A.1) for a range of R_i while tuning C_0. The best fit is obtained when $C_0 = 1$ (Fig. A.1).

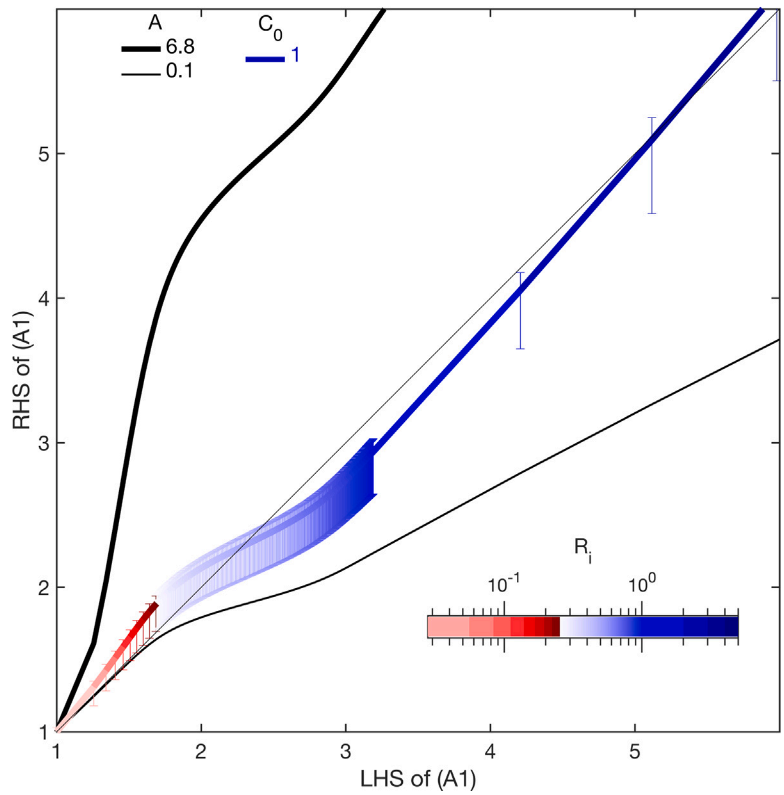

Fig. A.1. Best fit for the shape parameter α. Errorbar limits for the best fit is defined as $C_0 = 0.9, 1.03$ and colors denote R_i with regards to its critical value i.e., red for $R_i < 0.25$ and blue for $R_i > 0.25$. (For interpretation of the references to color in this figure legend, the reader is referred to the web version of this article.)

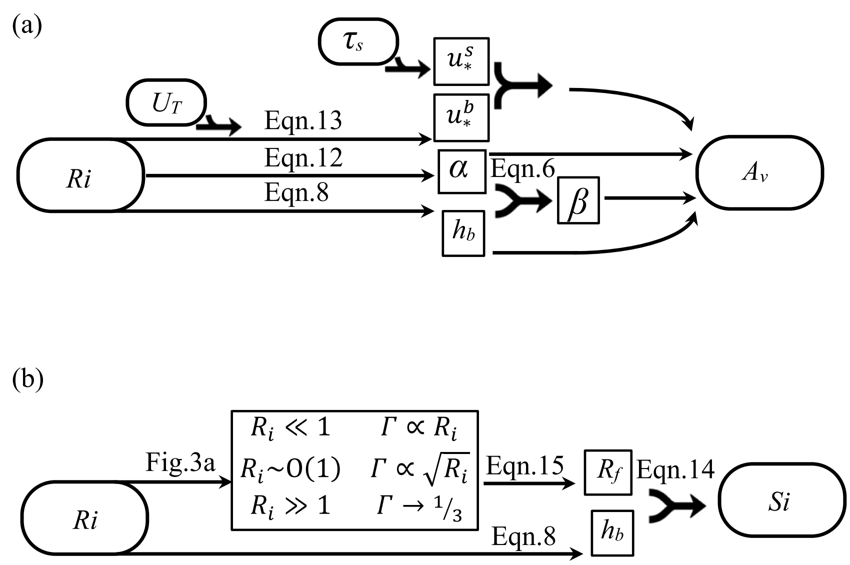

Fig. B.1. Flowchart describing the relation between R_i and (a) A_v profile, (b) S_i.

The term $1 + \kappa\sqrt{R_i}/c_b$ in (A.1) is analogous to the κ' (modified κ) ratio used in recent studies (Wang, 2002; Chen and De Swart, 2016) such that $\kappa/\kappa' = \left(1 + A \cdot R_f\right)$; written in terms of R_f and a constant A. Substituted in (A.1), its performance is tested for a range of $A = 0.1$–6.8 (i.e., lower and upper limits corresponding to the well-mixed and stratified conditions), respectively (Fig. A.1). The stability functions such as $\Psi_1 = \left(1 + A \cdot R_f\right)^{-1}$ and $\Psi_2 = \left(1 + A_1 \cdot R_i\right)^{A_2}$ depend on the constants A, A_1, and A_2 which differ from one system to another, while, $f(R_i)$ is based on physical variables thus providing an approach valid for all systems.

Appendix B. Flowchart of the developed analytical model

The A_v profile is obtained in terms of independent variables R_i, U_T, τ_s, z_0^s, and z_0^b. The procedure is summarized in Fig. B.1a. To solve (19), we need to know S_i. In a real estuary horizontal and vertical stratification (S_i and R_i) are interlinked. The R_i was chosen as the primary independent variable because compared to S_i it is easier to measure in the field. Therefore, S_i is obtained using R_i; a flowchart describing the approach is shown in Fig. B.1b.

Appendix C. Polynomial approximation

Depending on the degree of stratification, the eddy viscosity parameterized for the upper layer (4) becomes a function with fractional powers. This complicates the solution leading to fractional integrals. To overcome such complications, (4) can be approximated as a polynomial. This requires solving a system of equations that are expressed based on the gradients and values of $A_v^{T_U}$ at $z_{j=1...J}$.

$$A_v^{T_U}\left(z_j\right) = \sum_{i=1}^{n+1} p_{n-i+1} z_j^{n-i+1} \tag{C.1a}$$

$$\partial_z A_v^{T_U}\left(z_j\right) = \sum_{i=1}^{n} (n-i+1)\, p_{n-i+1} z_j^{n-i} \tag{C.1b}$$

Here, n is the polynomial degree and $p_0 ... p_n$ are the polynomial coefficients; the depths (z_j) correspond to critical points that determine the shape of $A_v^{T_U}$. These critical points are $z_1 = z_*$(equals 0 when $u_*^s \neq 0$, and $-z_0^s$ when $u_*^s = 0$) , $z_2 = z_m$, and $z_3 = -0.01H$. The degree of the approximation is chosen as $n = 5(n = 4)$ according to the intensity of the stratification i.e., $R_i > 0.5(R_i \leq 0.5)$. Next, the $n+1$ number of constraints and the associated equations will be expressed for each n separately. The equations are then solved for the polynomial coefficients.

C.1. Quartic polynomial approximation $(n = 4)$

$$\begin{bmatrix} z_1^n & \dots & z_1^0 \\ z_2^n & \dots & z_2^0 \\ nz_2^{n-1} & \dots\, z_2^0 & 0 \\ nz_3^{n-1} & \dots\, z_3^0 & 0 \end{bmatrix} \cdot \begin{bmatrix} p_4 \\ \vdots \\ p_0 \end{bmatrix} = \begin{bmatrix} A_v^{T_U}\left(z_1\right) \\ A_v^{T_U}\left(z_2\right) \\ \partial_z A_v^{T_U}\left(z_2\right) \\ \partial_z A_v^{T_U}\left(z_3\right) \end{bmatrix} \tag{C.2}$$

C.2. Quintic polynomial approximation $(n = 5)$

At $z = z_3$ both value and derivative are used as constraints to ensure that four turning points of the 5th degree polynomial-fit reside beyond the boundaries.

$$\begin{bmatrix} z_1^n & \dots & z_1^0 \\ z_2^n & \dots & z_2^0 \\ z_3^n & \dots & z_3^0 \\ nz_1^{n-1} & \dots\, z_1^0 & 0 \\ nz_2^{n-1} & \dots\, z_2^0 & 0 \\ nz_3^{n-1} & \dots\, z_3^0 & 0 \end{bmatrix} \cdot \begin{bmatrix} p_5 \\ \vdots \\ p_0 \end{bmatrix} = \begin{bmatrix} A_v^{T_U}\left(z_1\right) \\ A_v^{T_U}\left(z_2\right) \\ A_v^{T_U}\left(z_3\right) \\ \partial_z A_v^{T_U}\left(z_1\right) \\ \partial_z A_v^{T_U}\left(z_2\right) \\ \partial_z A_v^{T_U}\left(z_3\right) \end{bmatrix} \tag{C.3}$$

Appendix D. Analytical solution

The shape function γ in (19) can be expressed for upper and lower layers within $-1 \leq \tilde{z} \leq \tilde{z}_*$ where $\tilde{z}_* \approx -\tilde{z}_0^s$. The superscripts ^{U}, ^{L} denote the upper and the lower layers; the subscripts $_g$, $_w$, and $_r$ denote the density-driven, wind-driven and residual components, respectively. The expressions for the flow components can be written for each layer separately.

$$\gamma_r^L = \frac{\partial_{\tilde{z}}\chi_r^L - \partial_{\tilde{z}}\chi_r^L\big|_{\tilde{z}=-1}}{\chi_r\big|_{\tilde{z}=-1}^{\tilde{z}=\tilde{z}_*} - \sum_{\tilde{z}=-1}^{\tilde{z}_*}\partial_{\tilde{z}}\chi_r}$$
$$\gamma_r^U = \frac{\partial_{\tilde{z}}\chi_r^U + \partial_{\tilde{z}}\chi_r^L\big|_{\tilde{z}=\tilde{z}_m} - \partial_{\tilde{z}}\chi_r^L\big|_{\tilde{z}=-1} - \partial_{\tilde{z}}\chi_r^U\big|_{\tilde{z}=\tilde{z}_m}}{\chi_r\big|_{\tilde{z}=-1}^{\tilde{z}=\tilde{z}_*} - \sum_{\tilde{z}=-1}^{\tilde{z}_*}\partial_{\tilde{z}}\chi_r} \tag{D.1a}$$

$$\gamma_{g,w}^L = \partial_{\tilde{z}}\chi_{g,w}^L - \partial_{\tilde{z}}\chi_{g,w}^L\Big|_{\tilde{z}=-1} - \gamma_r^L\left(\chi_{g,w}\Big|_{\tilde{z}=-1}^{\tilde{z}=\tilde{z}_*} - \sum_{\tilde{z}=-1}^{\tilde{z}_*}\partial_{\tilde{z}}\chi_{g,w}\right)$$
$$\gamma_{g,w}^U = \partial_{\tilde{z}}\chi_{g,w}^U + \partial_{\tilde{z}}\chi_{g,w}^L\Big|_{\tilde{z}=\tilde{z}_m} - \partial_{\tilde{z}}\chi_{g,w}^L\Big|_{\tilde{z}=-1} - \partial_{\tilde{z}}\chi_{g,w}^U\Big|_{\tilde{z}=\tilde{z}_m} - \gamma_r^U\left(\chi_{g,w}\Big|_{\tilde{z}=-1}^{\tilde{z}=\tilde{z}_*} - \sum_{\tilde{z}=-1}^{\tilde{z}_*}\partial_{\tilde{z}}\chi_{g,w}\right) \tag{D.1b}$$

$$\sum_{\tilde{z}=-1}^{\tilde{z}_*}\partial_{\tilde{z}}\chi_{r,g,w} = (\tilde{z}_m+1)\,\partial_{\tilde{z}}\chi_{r,g,w}^L\Big|_{\tilde{z}=-1} - (\tilde{z}_*-\tilde{z}_m)(\partial_{\tilde{z}}\chi_{r,g,w}^L\Big|_{\tilde{z}=\tilde{z}_m} - \partial_{\tilde{z}}\chi_{r,g,w}^L\Big|_{\tilde{z}=-1} - \partial_{\tilde{z}}\chi_{r,g,w}^U\Big|_{\tilde{z}=\tilde{z}_m}) \tag{D.1c}$$

$$\chi_{r,g,w}\Big|_{\tilde{z}=-1}^{\tilde{z}=\tilde{z}_*} = \chi_{r,g,w}^L\Big|_{\tilde{z}=-1}^{\tilde{z}=\tilde{z}_m} + \chi_{r,g,w}^U\Big|_{\tilde{z}=\tilde{z}_m}^{\tilde{z}=\tilde{z}_*} \tag{D.1d}$$

Here, χ depends on the prescribed eddy viscosity profile and controls γ. The Eqs. (D.1a)–(D.1d) represent the base case where the eddy viscosity profile has not been defined yet, but assumed to vary with depth. These equations are derived based on the boundary conditions defined in Section 3.1. In the following, the shape functions for the eddy viscosity will be defined. This way, two approaches can be designed easily: (I) with direct application of the parameterization, and (II) with approximated parameterizations.

D.1. Restricted form with $u_*^s = 0$

When $u_*^s = 0$, explicit solution for upper and lower layers are listed as follows.

$$C^U = C_1\left(\tilde{h}_b-2\right)^{\alpha-1}\left(e^{1.386}\tilde{h}_b^{-\tilde{h}_b}\right)^{\alpha-1/\tilde{h}_b-2} \quad , \quad C_1 = \frac{\tilde{h}_b+\tilde{z}_0^b}{\kappa\left(\tilde{h}_b/2+\tilde{z}_0^b\right)^2} \tag{D.2a}$$

$$\chi_{g,r,w}^U(\tilde{z}) = C^U\frac{\tilde{z}^{\alpha_{g,r,w}^0-\alpha+1}}{\left(\alpha_{g,r,w}^0-\alpha\right)\left(\alpha_{g,r,w}^0-\alpha+1\right)} \times \tilde{\mathcal{F}}_{2,1}\left(\begin{matrix}\alpha_{g,r,w}^0-\alpha \quad , \quad \tilde{h}_b(1-\alpha)/(\tilde{h}_b-2) \\ \alpha_{g,r,w}^0-\alpha+2\end{matrix}\ \middle|\ -\tilde{z}\right) \tag{D.2b}$$

$$\chi_g^L(\tilde{z}) = \left\{-\tilde{z}\left(\tilde{z}-2\tilde{h}_b+4\right)\left(\tilde{h}_b/2+\tilde{z}_0^b\right) + \ln\left[\left(\tilde{z}-\tilde{h}_b-\tilde{z}_0^b+1\right)^{-\left(\tilde{h}_b+\tilde{z}_0^b-1\right)^2\left(\tilde{z}-\tilde{h}_b-\tilde{z}_0^b+1\right)} \times\left(\tilde{z}+\tilde{z}_0^b+1\right)^{\left(\tilde{z}_0^b+1\right)^2\left(\tilde{z}+\tilde{z}_0^b+1\right)}\right]\right\}C_1/2 \tag{D.2c}$$

$$\chi_r^L(\tilde{z}) = \left\{\tilde{z}\left(\tilde{h}_b+2\tilde{z}_0^b\right) - \ln\left[\left(\tilde{z}-\tilde{h}_b-\tilde{z}_0^b+1\right)^{\left(\tilde{h}_b+\tilde{z}_0^b-1\right)\left(\tilde{z}-\tilde{h}_b-\tilde{z}_0^b+1\right)} \times\left(\tilde{z}+\tilde{z}_0^b+1\right)^{\left(\tilde{z}_0^b+1\right)\left(\tilde{z}+\tilde{z}_0^b+1\right)}\right]\right\}C_1/2 \tag{D.2d}$$

$$\chi_w^L(\tilde{z}) = \ln\left[\left(\tilde{z}-\tilde{h}_b-\tilde{z}_0^b+1\right)^{-\left(\tilde{z}-\tilde{h}_b-\tilde{z}_0^b+1\right)}\left(\tilde{z}+\tilde{z}_0^b+1\right)^{\left(\tilde{z}+\tilde{z}_0^b+1\right)}\right]C_1/2 \tag{D.2e}$$

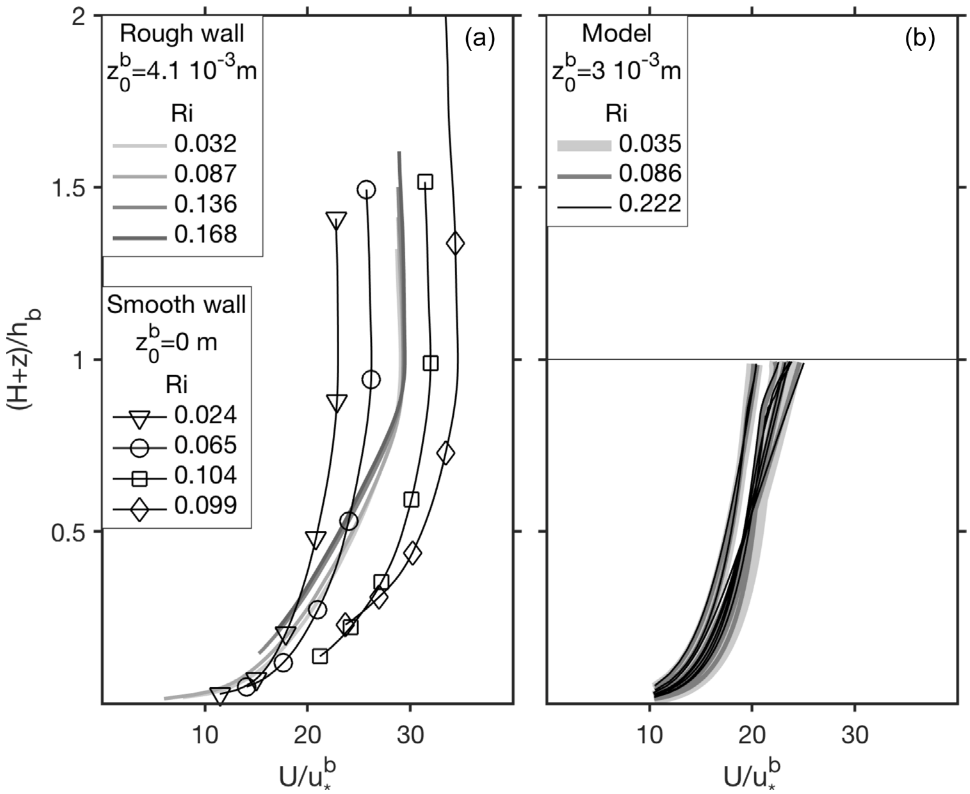

Fig. E.1. Log-law (a) Experimental study of turbulent boundary layer under stable thermal stratification adopted from Williams et al. (2017). (b) Model results.

In (D.2) $\alpha_g^0 = 4$, $\alpha_r^0 = 3$, and $\alpha_w^0 = 2$. Integer values of α result in infinity for which implicit solutions exist, but they are not shown. As $\tilde{z}_* \rightarrow 0$, the solution approaches infinity for the upper layer (D.2b) when $\alpha > \alpha^0_{g,r,w} + 1$.

D.2. Generalized form with polynomial approximation

The solution for χ, is obtained in terms of the roots of the polynomial (20), r_i with $i = 1 \ldots n$. Here, the approximated polynomials range from quadratic to quintic. Because the approximated polynomial has a turning point followed by a non-negative decreasing gradient with $z \rightarrow 0$, (20) has always at least one real root. Roots of the quintic polynomials have either one or two complex conjugate pairs. Roots of the quintic polynomial are obtained by reducing it to quartic form with its real root, and applying Ferrari's rule. MATHEMATICA or MATLAB can be used to find the roots of the polynomial.

$$\chi_g^U(\tilde{z}) = \sum_{i=1}^{n} r_i^2 a_i(\tilde{z}) \quad , \quad \chi_r^U(\tilde{z}) = \sum_{i=1}^{n} r_i a_i(\tilde{z}) \quad , \quad \chi_w^U(\tilde{z}) = \sum_{i=1}^{n} a_i(\tilde{z}) \qquad \text{(D.3)}$$

Here a_i is a function of z, r_i and the eddy viscosity gradient at $z = r_i$. When all roots of the polynomial are real numbers,

$$a_i(\tilde{z}) = \frac{\left(\tilde{z} - r_i\right) \ln\left(\tilde{z} - r_i\right) - \tilde{z}}{\partial_{\tilde{z}} A_v^{T_U}\Big|_{\tilde{z}=r_i}}. \qquad \text{(D.4)}$$

When some of the roots of the polynomial are conjugate pairs, the solution still consists of logarithmic functions analogous to (D.4) yet becomes more complex. For simplicity, this is not shown in here.

Appendix E. Validity of log-law

The validity of log law is explored within the bottom boundary layer. Williams et al. (2017) investigated the validity of the log-law within the turbulent boundary layer under thermal stratification by conducting lab experiments for small and rough walls. They observed a departure in the scaled velocity profiles for bulk Richardson numbers exceeding 0.1 for the smooth wall, and numbers exceeding 0.15 for the rough wall (Fig. E.1a). The model results with varying density stratification are shown in Fig. E.1b.

Appendix F. Skill assessment

Model skill assessment was carried out using a measure defined by Willmott (1981) to obtain a performance statistics for the exchange flow intensity $\widetilde{M}$ by comparing GOTM with analytical model results.

$$Skill = 1 - \frac{\sum \left|\widetilde{M}_{\text{Model}} - \widetilde{M}_{\text{GOTM}}\right|^2}{\sum \left(\left|\widetilde{M}_{\text{Model}} - \overline{\widetilde{M}}_{\text{GOTM}}\right| + \left|\widetilde{M}_{\text{GOTM}} - \overline{\widetilde{M}}_{\text{GOTM}}\right|\right)^2} \qquad \text{(F.1)}$$

Perfect agreement yields a skill of one and complete disagreement yields a skill of zero.

The exchange flow intensity associated with (19) shows good agreement only for $|W.Si| < 0.2$ (dotted markers, Fig. 9a, d, g). For bigger wind stress the model results in overestimates $\widetilde{M}_{\text{Model}} \approx 1.67\widetilde{M}_{\text{GOTM}}$. Because wind entrainment and wind adjustment to vertical stratification are ignored in A_v^T, (19) yields overestimates in exchange flow intensity. When the contribution of wind driven component of the exchange flow is reduced in half $\tilde{U}_w/2$, the skill index approaches 1.

In addition, the analytical solution ignores tidal variations in eddy viscosity profiles yielding underestimates in the exchange flow profiles and intensity. With decreasing unsteadiness number i.e., increasing tidal current amplitude the tidal variability in A_v^T increases, so does its contribution to the exchange flow. This effect is approximated by modifying the contribution of density driven component to the exchange flow. For the low tidal amplitude, the skill index reaches 1 with U_g (Fig. 9a), while for relatively strong tidal current amplitudes the higher skill index is achieved with $2U_g, 3U_g$ (Fig. 9e, h, i).

References

Basdurak, N., Huguenard, K., Valle-Levinson, A., Li, M., Chant, R., 2017. Parameterization of mixing by secondary circulation in estuaries. J. Geophys. Res.: Oceans 122 (7), 5666–5688.

Burchard, H., Hetland, R.D., 2010. Quantifying the contributions of tidal straining and gravitational circulation to residual circulation in periodically stratified tidal estuaries. J. Phys. Oceanogr. 40 (6), 1243–1262.

Burchard, H., Hetland, R.D., Schulz, E., Schuttelaars, H.M., 2011. Drivers of residual estuarine circulation in tidally energetic estuaries: Straight and irrotational channels with parabolic cross section. J. Phys. Oceanogr. 41 (3), 548–570.

Canuto, V.M., Howard, A., Cheng, Y., Dubovikov, M., 2001. Ocean turbulence. Part i: One-point closure model—Momentum and heat vertical diffusivities. J. Phys. Oceanogr. 31 (6), 1413–1426.

Chant, R.J., Geyer, W.R., Houghton, R., Hunter, E., Lerczak, J., 2007. Estuarine boundary layer mixing processes: Insights from dye experiments. J. Phys. Oceanogr. 37 (7), 1859–1877.

Charnock, H., 1955. Wind stress on a water surface. Q. J. R. Meteorol. Soc. 81 (350), 639–640.

Chen, W., De Swart, H.E., 2016. Dynamic links between shape of the eddy viscosity profile and the vertical structure of tidal current amplitude in bays and estuaries. Ocean Dyn. 66 (3), 299–312.

Chen, S.-N., Sanford, L.P., 2009. Axial wind effects on stratification and longitudinal salt transport in an idealized, partially mixed estuary. J. Phys. Oceanogr. 39 (8), 1905–1920.

Cheng, P., de Swart, H.E., Valle-Levinson, A., 2013. Role of asymmetric tidal mixing in the subtidal dynamics of narrow estuaries. J. Geophys. Res.: Oceans 118 (5), 2623–2639.

Cheng, P., Valle-Levinson, A., de Swart, H.E., 2011. A numerical study of residual circulation induced by asymmetric tidal mixing in tidally dominated estuaries. J. Geophys. Res.: Oceans 116 (C1).

Craig, P.D., Banner, M.L., 1994. Modeling wave-enhanced turbulence in the ocean surface layer. J. Phys. Oceanogr. 24 (12), 2546–2559.

Dijkstra, Y.M., Schuttelaars, H.M., Burchard, H., 2017. Generation of exchange flows in estuaries by tidal and gravitational eddy viscosity-shear covariance (ESCO). J. Geophys. Res.: Oceans 122 (5), 4217–4237.

Dyer, K., Soulsby, R., 1988. Sand transport on the continental shelf. Annu. Rev. Fluid Mech. 20 (1), 295–324.

Garanaik, A., Venayagamoorthy, S.K., 2019. On the inference of the state of turbulence and mixing efficiency in stably stratified flows. J. Fluid Mech. 867, 323–333.

Geyer, W.R., MacCready, P., 2014. The estuarine circulation. Annu. Rev. Fluid Mech. 46.

Geyer, W.R., Trowbridge, J.H., Bowen, M.M., 2000. The dynamics of a partially mixed estuary. J. Phys. Oceanogr. 30 (8), 2035–2048.

Hansen, D.V., Rattray, M., 1965. Gravitational circulation in straits and estuaries. J. Mar. Res. 23.

Ianniello, J., 1977. Tidally induced residual currents in estuaries with constant breadth and depth. J. Mar. Res. 35, 755–786.

Lange, X., Burchard, H., 2019. The relative importance of wind straining and gravitational forcing in driving exchange flows in tidally energetic estuaries. J. Phys. Oceanogr. 49 (3), 723–736.

Li, M., Trowbridge, J., Geyer, R., 2008. Asymmetric tidal mixing due to the horizontal density gradient. J. Phys. Oceanogr. 38 (2), 418–434.

Maffioli, A., Brethouwer, G., Lindborg, E., 2016. Mixing efficiency in stratified turbulence. J. Fluid Mech. 794.

McGregor, R., 1972. The influence of eddy viscosity on the vertical distribution of velocity in the tidal estuary. Geophys. J. 29, 103–108.

Monismith, S.G., Burau, J.R., Stacey, M., 1996. Stratification dynamics and gravitational circulation in northern san francisco bay. San Francisco Bay: Ecosyst. 123–153.

Peters, H., Bokhorst, R., 2001. Microstructure observations of turbulent mixing in a partially mixed estuary. part ii: Salt flux and stress. J. Phys. Oceanogr. 31 (4), 1105–1119.

Purkiani, K., Becherer, J., Klingbeil, K., Burchard, H., 2016. Wind-induced variability of estuarine circulation in a tidally energetic inlet with curvature. J. Geophys. Res.: Oceans 121 (5), 3261–3277.

Ralston, D.K., Geyer, W.R., Lerczak, J.A., 2008. Subtidal salinity and velocity in the hudson river estuary: Observations and modeling. J. Phys. Oceanogr. 38 (4), 753–770.

Shih, L.H., Koseff, J.R., Ivey, G.N., Ferziger, J.H., 2005. Parameterization of turbulent fluxes and scales using homogeneous sheared stably stratified turbulence simulations. J. Fluid Mech. 525, 193–214.

Simpson, J.H., Brown, J., Matthews, J., Allen, G., 1990. Tidal straining, density currents, and stirring in the control of estuarine stratification. Estuaries 13 (2), 125–132.

Stacey, M.T., Brennan, M.L., Burau, J.R., Monismith, S.G., 2010. The tidally averaged momentum balance in a partially and periodically stratified estuary. J. Phys. Oceanogr. 40 (11), 2418–2434.

Stacey, M.T., Burau, J.R., Monismith, S.G., 2001. Creation of residual flows in a partially stratified estuary. J. Geophys. Res.: Oceans 106 (C8), 17013–17037.

Strang, E., Fernando, H., 2001. Entrainment and mixing in stratified shear flows. J. Fluid Mech. 428, 349–386.

Taylor, J.R., Sarkar, S., 2008. Stratification effects in a bottom ekman layer. J. Phys. Oceanogr. 38 (11), 2535–2555.

Umlauf, L., Burchard, H., 2005. Second-order turbulence closure models for geophysical boundary layers. a review of recent work. Cont. Shelf Res. 25 (7–8), 795–827.

Venayagamoorthy, S.K., Koseff, J.R., 2016. On the flux richardson number in stably stratified turbulence. J. Fluid Mech. 798.

Wang, X.H., 2002. Tide-induced sediment resuspension and the bottom boundary layer in an idealized estuary with a muddy bed. Journal of Physical Oceanography 32 (11), 3113–3131.

Werner, S.R., Beardsley, R.C., Lentz, S.J., Hebert, D.L., Oakey, N.S., 2003. Observations and modeling of the tidal bottom boundary layer on the southern flank of georges bank. J. Geophys. Res.: Oceans 108 (C11).

Williams, O., Hohman, T., Van Buren, T., Bou-Zeid, E., Smits, A.J., 2017. The effect of stable thermal stratification on turbulent boundary layer statistics. J. Fluid Mech. 812, 1039–1075.

Willmott, C.J., 1981. On the validation of models. Phys. Geogr. 2 (2), 184–194.

Zitman, T.J., Schuttelaars, H.M., 2012. Importance of cross-channel bathymetry and eddy viscosity parameterisation in modelling estuarine flow. Ocean Dyn. 62 (4), 603–631.